2012

Three-color Coherent Anti-Stokes Raman Scattering: from tracing dynamics of elementary excitations in solids to imaging of live cells.

Manoj Kumar Dobbala

Recommended Citation

Dobbala, Manoj Kumar, "Three-color Coherent Anti-Stokes Raman Scattering: from tracing dynamics of elementary excitations in solids to imaging of live cells." (2012). *Graduate Theses, Dissertations, and Problem Reports*. 12289.
https://researchrepository.wvu.edu/etd/12289

Three-color Coherent Anti-Stokes Raman Scattering: from tracing dynamics of elementary excitations in solids to imaging of live cells.

Manoj Kumar Dobbala

Thesis submitted to the
Benjamin M. Statler College of Engineering and Mineral Resources at West Virginia University
In partial fulfillment of the requirements for the degree of

Master of Science
in
Mechanical Engineering

Feruz Ganikhanov, Ph.D., Chair

Darran R. Cairns, Ph.D., Co-Chair

Nithi T. Sivaneri, Ph.D.

Department of Mechanical and Aerospace Engineering
Morgantown, West Virginia
2012

Keywords: CARS, Nonlinear Susceptibility, Microscopy, Spectroscopy

ProQuest LLC.
789 East Eisenhower Parkway
P.O. Box 1346
Ann Arbor, MI 48106 - 1346

`

ABSTRACT

Three-color Coherent Anti-Stokes Raman Scattering: from tracing dynamics of elementary excitations in solids to imaging of live cells.

Manoj kumar Dobbala
Master of Science in Mechanical Engineering, West Virginia University
Dr. Feruz Ganikhanov, Ph.D., Chair

Commonly used laser based spectroscopy and imaging techniques have both advantages and disadvantages. Therefore, a system that allows access to molecularly specific properties is highly desired. The primary objective of the study is to demonstrate state-of-the art for coherent laser spectroscopy and microscopy and their applications in biomedical imaging and condensed matter characterization. This study also demonstrates the capabilities and application of time-domain coherent spectroscopy technique to characterize soft- (aqueous media, large organic molecules and biological media) and traditional condensed matter (including solid state crystals, inorganic microstructures and photonic materials). Work on coherent multi-photon microscopy and approaches concerned to the experimental realization of femtosecond time domain '**C**oherent **A**nti-**S**tokes **R**aman Scattering **S**pectroscopy' (CARS) are demonstrated.

Problems and issues related to generation of broadly tunable femtosecond optical parametric oscillators (OPOs) based on periodically poled lithium Tantalate crystal, Experimental realization of human blood sample, tracing phonon dynamics and elementary excitations in KTP crystal and its decay time are presented.

`

Dedicated to my parents, Apparao and Vijayalaxmi, and my Brother Karthik

Acknowledgements

I would like to thank everyone who helped and supported me during the progress of this research. I am greatly thankful to my advisor, Dr. Feruz Ganikhanov for his constant support and guidance during the graduate studies at WVU. His enthusiasm for research and patience demonstrated during the set up of the experiments helped maintain an exciting and productive research environment. I would like to thank my co-advisor Dr. Darran Cairns for mentoring me during the years at WVU. I would like to thank Dr. Nithi Sivaneri for his constant support and valuable feedback in all aspects of my study.

I would like to sincerely thank all the students, past and present, at the Ultrafast Optics Laboratories, Without their help and support, this thesis would not have be possible. Some of the Ultrafast Optics lab-mates are Shan Yang, Sanjay Adhikari, Vivek kosgi and Uday Arredla.

I would like to thank my friends at WVU Praneeth, Sodith, Ravi, Sriram, Sai Praneeth, Vijay, Chintu Nani and Sasi for making graduate life so much fun.

My special Thanks to my friends Dheeraj, Naresh, Karthik, Bharath, Ajay, Sivaram and Soumya who have been my source of inspiration with their continuous support and encouragement in every aspects of my life.

Funding for this work was provided by National Science Foundation (NSF) under Cooperative Agreement Number NSF ECCS-0925437.

Table of Contents

`

List of Figures

`

`

`

Nomenclature

OPO	Optical Parametric Oscillator
CARS	Coherent Anti Stokes Raman Scattering
KTP	Potassium Titanyl phosphate
F-CARS	Forward-CARS
E-CARS	Epi - CARS
P-CARS	Polarized –CARS
T-CARS	Time domain-CARS
SHG	Second Harmonic Generation
THG	Third Harmonic Generation
VI	Virtual Instrument
Fs	Femto second Pulses,
Ps	Pico second Pulses

`

Chapter 1

Introduction

1.1. Introduction.

Spectroscopic techniques that have been developed during past decades to measure dispersion of absorption and refractive indices in the infrared (IR), visible (VIS) and ultraviolet (UV) wavelength ranges are at the core of the condensed matter spectroscopy field. The response of a medium in that case is due to optical polarization induced by incident light fields. The induced polarization can be a source of new light and provide new information about the medium under study.

The presented work focuses entirely on the nonlinear spectroscopic techniques that help to obtain valuable spectroscopic information with high resolution and sensitivity in optical frequency, time and space domains.

Let us consider polarization of a medium in response to the applied electric field $\vec{E}(t)$. We will consider $\vec{E}(t)$ to be a plane wave which can be formalistically presented as:

$$\vec{E}(z,t) = \vec{E}_0 e^{-i(\omega t - kz)} + c.c \tag{1}$$

Where $\vec{E}_0$ is amplitude, ω - optical frequency, k - wave vector where $k = \frac{\omega}{c} n$

In a traditional linear absorption or refractive index measurement spectroscopies the electromagnetic field is considered to be weak in a sense that it does not cause any perturbation to the atomic/molecular potential. In other words and quantitatively, the incident field is negligible compared to the atomic E_{at}= 2 x 10^7 *stat volt/cm*[1]. This results in a polarization to be a linear function of the applied field. Namely, the polarization can be represented as follows:

$$\vec{P}(t) = \chi^{(1)} \vec{E}(t) \tag{2}$$

Where $\vec{P}(t)$ can be considered as material macroscopic dipole moment per unit volume. Applying a simple classical model of a harmonic oscillator at a resonant frequency ω_0 yields in

$\chi^{(1)}$ or linear susceptibility of which dispersion near the optical frequency resonance ω_n can be expressed in the following relationship [1]:

$$\chi^{(1)}(\omega) = \frac{Ne^2 / m_0}{\left(\omega_0^2 - \omega^2 - 2i\omega\,\gamma\right)} \tag{3}$$

Where N-number of molecules per unit volume, e-electron charge, m_0- mass of electron, γ-damping factor

Obviously, $\chi^{(1)}$ has a real and imaginary part and the two are responsible for dispersion of the corresponding absorption and refractive index. As an example we can consider a simple case of the harmonic oscillator. The dispersion of real and imaginary parts of $\chi^{(1)}$ are shown below.

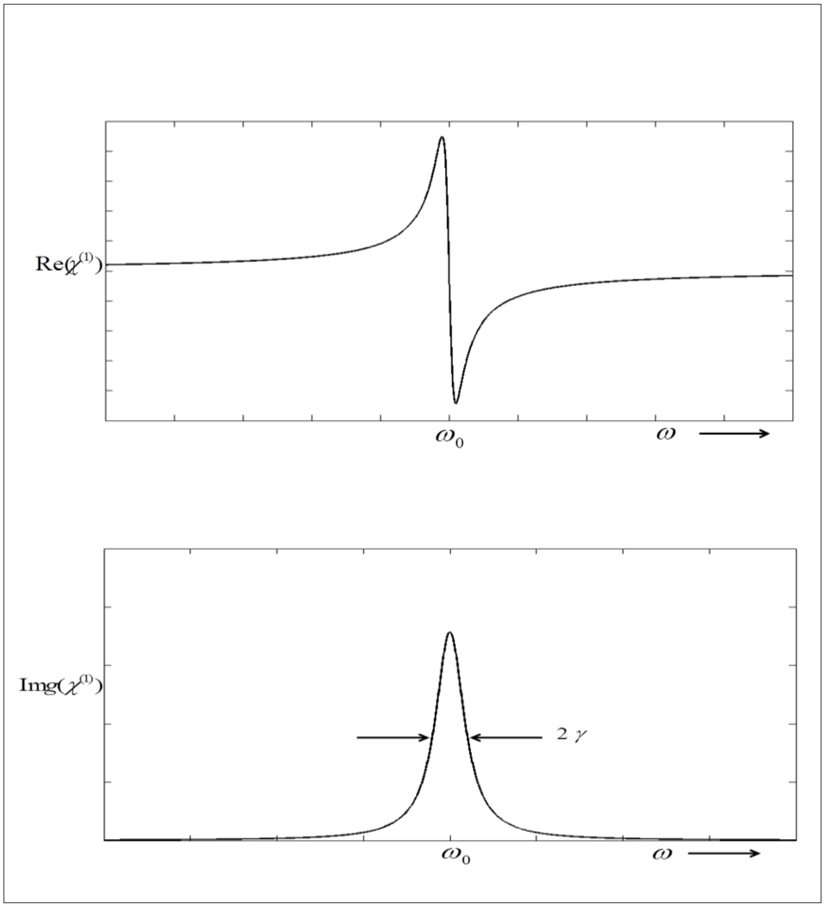

Figure 1: Dispersion of the real and imaginary part of $\chi^{(1)}$ calculated using a harmonic oscillator model (see formula 3)

`

The absorption coefficient (alpha) and refractive index of a medium relate to the real and imaginary parts of $\chi^{(1)}$ as follows:

$$\text{Refractive index } (n) = \sqrt{\varepsilon} = \sqrt{1 + \mathrm{Re}\left(\chi^{(1)}\right)} \tag{4}$$

$$\text{Absorption Coefficient } (\alpha) = \frac{2\pi}{\lambda n} \mathrm{Im}\left(\chi^{(1)}\right) \tag{5}$$

Where λ is the incident beam's wavelength in vacuum. The two characteristics are connected to each other via Kramers-Kronig relations[1]. Again, this relationship is valid if the electric field is much weaker than the inter-atomic field E_{at}.

1.2. Nonlinear polarization

As the intensities of the applied electric field increases the polarization due to nonlinear susceptibilities starts to contribute noticeably. Then, in general, we can write for the total polarization the following:

$$\vec{P} = \vec{P}^{L} + \vec{P}^{NL} = \varepsilon_0 \left[\chi^{(1)} \cdot \vec{E} + \chi^{(2)} \cdot \vec{E} \cdot \vec{E} + \chi^{(3)} \cdot \vec{E} \cdot \vec{E} \cdot \vec{E}\right] \tag{6}$$

In the expression above, $\vec{P}^{NL}$ is a contribution to the overall polarization that is not linear in terms of the incident field(s). The ratio of the inter-atomic electric field to the incident one can be considered as an indicative parameter for evaluation of the nonlinear polarization contributions to the total polarization $\vec{P}$. The inter-atomic field can be estimated using Bohr's atomic model. Namely,

$$E_{at} = \frac{e}{\left(4\pi\varepsilon_0 a_0^2\right)} \tag{7}$$

Where, Bohr's radius $a_0 = \dfrac{4\pi\varepsilon_0\hbar^2}{m_0 e^2}$, e stand for electron charge, m_0 is mass of electron, and $\hbar$ is Plank's constant. Thus, $E_{at} \approx 3\times10^{8}\dfrac{V}{cm}$.

One can straightforwardly estimate the incident field parameters in order to approach the intensity levels that are comparable to E_{at}. The above intensity can be easily achieved using pulsed lasers and tight beam focusing. For example, for 100 *fs* wide pulses (t_p) from a mode-locked laser delivering average power (P_{avg}) of 1 *W* at a repetition rate of (ν) 100 *MHz* and applying high numerical aperture (NA) beam focusing we arrive to the peak intensities of

$$I = \frac{\varepsilon}{t_p}\frac{1}{\pi w^2} = 1.4\times 10^{14}\,\frac{W}{cm^2} \tag{8}$$

Where, ε is an isolated pulse energy $\left(\varepsilon = {}^{P_{avg}}\!\big/_{\nu}\right)$=10*nJ*), w-incident beam radius at foci (~150 nm for NA~1 in visible wavelength range).

Thus, the corresponding electric field in foci is calculated according to the expression below.

$$E = \left(\frac{4\pi\cdot I}{c}\right)^{1/2} \cong 2\times 10^{8}\,\frac{V}{cm} \tag{9}$$

Thus, the ratio E/Eat= 2/3, or just at inter atomic field level and therefore nonlinear terms cannot be neglected anymore in equation (6).

Now, let us assume that the total polarization can be represented in power series of the incident field. Namely,

$$\begin{aligned}\vec{P}(t) &= \chi^{(1)}\vec{E}(t) + \chi^{(2)}\vec{E}^{(2)}(t) + \chi^{(3)}\vec{E}^{(3)}(t) + \ldots\\ &= \vec{P}^{(1)}(t) + \vec{P}^{(2)}(t) + \vec{P}^{(3)}(t) + \ldots\ldots\end{aligned} \tag{10}$$

In the equation above, $\chi^{(2)}, \chi^{(3)}$, …,etc. are higher order nonlinear susceptibilities. Using the same harmonic oscillator model we can estimate ratios of ${}^{\chi^{(2)}}\!\big/_{\chi^{(1)}}, {}^{\chi^{(3)}}\!\big/_{\chi^{(2)}}$ ...., etc.[1, 2]. More rigorous approach of calculating the susceptibilities is based on the density matrix approach using a perturbation quantum mechanical theory [3]. The results are presented in a numerous and extensive studies of this topic[4, 5]. Following the rigorous approach outlined in

`

those works brings us to a conclusion that $\chi^{(2)}$ is non-zero only for a certain class of materials. Namely, $\chi^{(2)}$ is non-zero for materials with a lack of center of symmetry. The second order susceptibility vanishes for centrosymmetric media. Therefore $\chi^{(2)}$ based nonlinear spectroscopy [6] has limited applications since it is suitable for characterization of only non-centrosymmetric media. The third order susceptibility is generally nonzero for any material. Thus, in principal, $\chi^{(3)}$ based spectroscopic characterization of media is of great interest in condensed matter studies. I will focus entirely on the third order nonlinear processes characterized by its susceptibility $\chi^{(3)}$.

1.3. Third order nonlinear polarization for different processes.

$\chi^{(3)}$ is a third order nonlinear optical susceptibility that is generally a fourth rank tensor that has 81 elements . Only 21 out of the 81 tensor elements are non zero for isotropic materials [1]. Let us assume that the input electric fields consist of waves at different optical frequencies. Thus, the resulting field incident on the medium is

$$\vec{E} = \vec{E}_1 + \vec{E}_2 + \vec{E}_3 \tag{11}$$

Where, the fields $\vec{E}_1, \vec{E}_2, \vec{E}_3$ oscillate at carrier frequencies $\omega_1, \omega_2, \omega_3$. Based on what has been assumed above (*see formula (11)*), the corresponding nonlinear contribution to the overall polarization due to the third order processes can be expressed by the following formula:

$$\vec{P}^{(3)}(t) = \chi^{(3)} : \vec{E}_1(t)\vec{E}_2(t)\vec{E}_3(t) \tag{12}$$

As was mentioned in the Introduction, the nonlinear polarization acts as a source of a new radiation. The intensity of the resulting new wave, due to the nonlinear polarization, depends, in particular, on an efficient interaction of the four waves. Namely, a new signal wave at ω_4 frequency and the three incident waves should interact under certain phase relationships between them in a dispersive medium. We will consider the process of generation of the new field at ω_4 using Maxwell equations approach and the details of this will be given below.

`

At this point, I would like to describe a process of third harmonic generation. This can be done formalistically by just considering a case when the incident frequencies of the three waves are the same. Effectively this is the situation when we have one incident field at frequency ω. For a linearly polarized incident field the nonlinear polarization responsible for the third harmonic generation process can be represented by the following formula:

$$P^{(3)}(3\omega) = \chi^{(3)}(3\omega;\omega,\omega,\omega)E^{(3)}(\omega) \qquad (13)$$

Here, again, $\chi^{(3)}$ stands for the corresponding nonlinear optical susceptibility. The process can be shown on the following energy diagram where an example of an atomic medium is considered. On this diagram we also assume that the incident photon energy is in close resonance with multiple atomic energy levels.

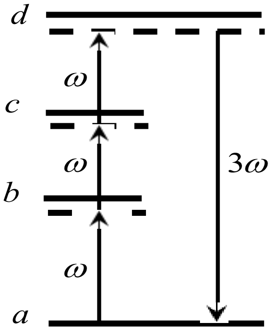

Figure 2: Quantum diagram for third harmonic generation process in atomic medium with energy levels closely matching the incident field photon energy.

The nonlinear optical susceptibility can be calculated using quantum mechanical perturbation theory. Assuming that ω is in resonance with ω_{ab} , ω_{bc} and ω_{cd} , we get a resonant enhancement of $\chi^{(3)}$ which can now be represented as follows:

$$\chi^{(3)}_{xxxx}(3\omega,\omega,\omega,\omega) = \frac{N}{\hbar^3}\frac{\mu^k_{ad}\mu^j_{dc}\mu^i_{cb}\mu^h_{ba}}{[(\omega_{da}-3\omega)-i\gamma_{da}][(\omega_{ca}-2\omega)-i\gamma_{ca}][(\omega_{ba}-\omega)-i\gamma_{ba}]} \qquad (14)$$

We assumed that the field is linearly polarized and is along x-axis with respect to the atomic system. μ_{ab} is a linear transition dipole moment between states a and b, etc. γ_{ab} is a corresponding damping factor that takes into account finite energy width of the atomic levels.

For THG process investigated in alkaline metal vapors authors of Ref. [7] presented theoretical calculations that predicted that the combination of near infrared susceptibilities, the ability to phase-match and ultraviolet transparency of alkaline metal vapors produce potentially high conversion efficiency in the THG process. Third order nonlinear susceptibility was calculated and the results are plotted as a function of incident wavelengths for each of the alkaline metal vapors. *Figure 3* shows the calculated results for sodium atom vapors.

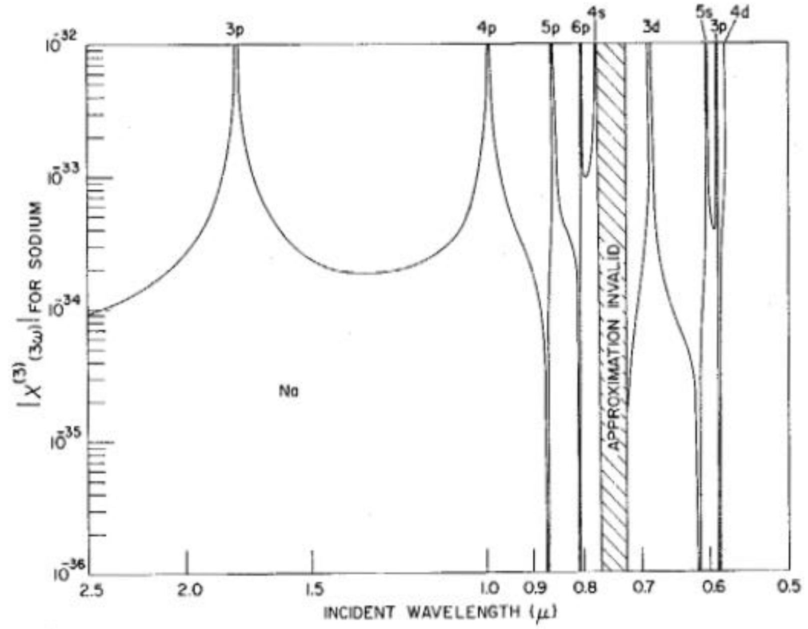

Figure 3: Nonlinear susceptibility of sodium versus incident wavelength.

Since atomic vapors is an example of centrosymmetric system they, as was mentioned above, cannot produce a response due to second order nonlinearity $\chi^{(2)}$. It is found that Incident wavelength of $\approx 1.8\mu m$ is required to attain the peak at $10^{-32} esu$ for $\chi^{(3)}(3\omega)$ at $3p(3\omega)$ due to three photon resonance with $3p$ level of sodium. Authors made several conclusions and indicated on limitations based on their experimental results for the efficient third harmonic generation. Reduction of phase matching ratio can be achieved by replacing the inert gas with a media with higher refractive index per atom. Use of molecular quenching agent such as N_2 or H_2 can reduce the atomic delay time. Use of multi-pass techniques combined with tight focusing geometry result in nearly phase-matched condition [7].

`

Considering again a more general case, when all the four fields are different, one finds that several wave mixing processes are possible. Some of the non-degenerate wave-mixing processes are listed below.

$$\begin{aligned} P^{(3)}(\omega_4;\omega_1+\omega_2+\omega_3) &= 6\varepsilon_0\chi^{(3)}E_1E_2E_3, \\ P^{(3)}(\omega_1+\omega_2-\omega_3) &= 6\varepsilon_0\chi^{(3)}E_1E_2E_3^*, \\ P^{(3)}(\omega_1+\omega_3-\omega_2) &= 6\varepsilon_0\chi^{(3)}E_1E_3E_2^*, \\ P^{(3)}(\omega_2+\omega_3-\omega_1) &= 6\varepsilon_0\chi^{(3)}E_2E_3E_1^*, \end{aligned} \tag{15}$$

As concerned degenerate processes, the following nonlinear polarizations are relevant:

$$\begin{aligned} P^{(3)}(2\omega_1+\omega_2) &= 3\varepsilon_0\chi^{(3)}E_1^2E_2, \\ P^{(3)}(2\omega_2+\omega_1) &= 3\varepsilon_0\chi^{(3)}E_2^2E_1, \\ P^{(3)}(2\omega_3+\omega_1) &= 3\varepsilon_0\chi^{(3)}E_3^2E_1, \\ P^{(3)}(2\omega_1-\omega_2) &= 3\varepsilon_0\chi^{(3)}E_1^2E_2^*, \\ P^{(3)}(2\omega_2-\omega_1) &= 3\varepsilon_0\chi^{(3)}E_2^2E_1^*, \\ P^{(3)}(2\omega_3-\omega_1) &= 3\varepsilon_0\chi^{(3)}E_3^2E_1^*, \end{aligned} \tag{16}$$

As was mentioned above, the main focus of this thesis is on process that is called Coherent Anti-Stokes Raman Scattering (CARS). The technique is used to investigate Raman active resonances and modes. In this process, in general, one deals with three different incident waves at frequencies $\omega_1,\omega_2,\omega_3$. If we assume that $\omega_3>\omega_2>\omega_1$, then the interaction that represents CARS would be one that is governed by the following nonlinear polarization:

$$\vec{P}^{(3)}(\omega_4;\omega_2-\omega_1+\omega_3) = 6\varepsilon_0\chi^{(3)} : \vec{E}_2\vec{E}_1^{\,*}\vec{E}_3 \tag{17}$$

Here, we assumed a general case of arbitrarily polarized incident fields. Thus, the product before the fields has to be considered as a tensor product. The corresponding third order susceptibility $\chi^{(3)}(\omega_4;\omega_2,-\omega_1,\omega_3)$ is resonantly enhanced when a Raman mode frequency (Ω) is close to $(\omega_2-\omega_1)$ frequency.

As can be seen from the expression above, during the CARS process, a new wave at $\omega_4 = \omega_3 + (\omega_2 - \omega_1)$ is generated. This new wave is called anti-Stokes wave at optical frequency $\omega_{as} = \omega_4$. Opposite to that case, when $\omega_4 = \omega_3 - (\omega_2 - \omega_1)$ one deals with Coherent Stokes Raman Scattering (CSRS),which is almost an identical process except for the fact that Stokes wave is detected which is at a lower optical frequency $\omega_{as} = \omega_4$ shifted by Ω from ω_3. Details of corresponding theoretical considerations will follow just below. CARS process in the case of the incident waves at two different frequencies represent a degenerate case. In this case, and assuming that we only supply waves at ω_1 and ω_2 CARS process is described by the following nonlinear polarization (linearly polarized beams with identical polarizations are considered here):

$$P^{(3)}(2\omega_1 - \omega_2) = 3\varepsilon_0 \chi^{(3)}(\omega_{as}; \omega_1, -\omega_2, \omega_1) E_1^2 E_2^* \tag{18}$$

1.4. Photon energy diagram for CARS.

As was mentioned above, in case when the incident wave frequencies for the optical fields are different $(\omega_3 > \omega_2 > \omega_1)$ the resulting signal wave frequency and the corresponding nonlinearity are the following:

$$\begin{gathered} \omega_{signal} = \omega_2 - \omega_1 + \omega_3; \\ \chi^{(3)}\left(\omega_{signal}, -\omega_1, \omega_2, \omega_3\right) \end{gathered} \tag{19}$$

Let us consider an atomic or molecular system with a transition $a \rightarrow b$ being Raman active only. Thus for this system $\omega_{ab} = \Omega$. From a quantum mechanical point of view a direct transition from state *a* to state *b* is forbidden in this case.

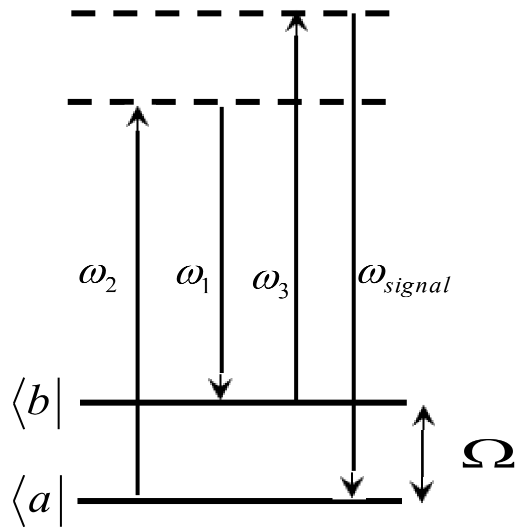

Figure 4: Quantum diagram for Coherent Anti Stokes Raman Scattering.

Interaction of photons in CARS process can be presented on the energy diagram above. Based on this diagram, CARS can be described as two-photon ‘excitation’ process followed by a two-photon ‘de-excitation’ process. Combined together the two constitute a resonantly enhanced (due to a and b quantum energy levels) four-wave mixing process. In an experiment, a degenerate CARS process is realized with at least two laser beams with strong intensity. The first beam at optical frequency ω_2 is often called ‘Pump’ and the second with frequency ω_1 is called ‘Stokes’ beam. Both beams are focused simultaneously onto a sample. We again note that $\omega_2 > \omega_1$. The incident beams excite the corresponding Raman active transition formed by states with energy levels E_a and E_b. The same beam at ω_2 will also serve, for this particular case, as a third or probe beam with frequency $\omega_3 = \omega_2$. The beam is scattered off the excited vibrations to form a wave with frequency $\omega_4 = \omega_2 - \omega_1 + \omega_2 = 2\omega_2 - \omega_1$ which is an anti-stokes frequency that is $\Omega = \omega_2 - \omega_1$ shifted from ω_2. The new wave is resonantly enhanced since frequency difference $\omega_2 - \omega_1$ is matched to Ω as was just mentioned.

$$\Omega = \omega_2\ (pump)\text{-}\ \omega_1\ (stokes) \tag{20}$$

$$\omega_4\ (Anti\text{-}stokes) = \omega_2\ (pump) + \omega_3\ (probe) - \omega_1(stokes)) \tag{21}$$

Thus, anti-Stokes wave in the CARS process will follow at frequency

$$\omega_{as} = 2\omega_2 - \omega_1 \tag{22}$$

If ω_2 frequency is tunable a dispersion of the corresponding $\chi^{(3)}(\omega_{as};\omega_2,-\omega_1,\omega_2)$ can be measured by detecting anti-Stokes wave’s intensity. I will show that explicitly in the following sections. Initially, the practical realization of this opportunity was hampered by a lack of suitable sources of tunable radiation. Recently, with the development of high-power tunable lasers, the utility of the technique was greatly enhanced and its applicability in various fields has rapidly expanded.

General expressions for the nonlinear polarization responsible for CARS signal are derived further below (*section 1.5*). The nonlinear polarization is used as a driving force in Maxwell’s equations for the anti-Stokes field. In general, a set of coupled-wave equations involving ‘Pump’, ‘Stokes’ and anti-Stokes waves should be solved in order to obtain the coherent anti-stokes field amplitude and the corresponding intensity.

1.5. CARS signal intensity and the phase-matching condition.

CARS signal is generated due to the interaction of atomic/molecular Raman active vibrations with light. The interaction is governed by a nonlinear polarization $P_i^{(3)CARS}$ that can be expressed using the following relationship:

$$P_i^{(3)CARS}(\omega_{as}) = \varepsilon_0 \chi_{ijkl}^{(3)CARS} E_j(\omega_3) E_k(\omega_2) E_l^*(\omega_1) \tag{23}$$

Resonant part of the third order nonlinearity can be expressed near a vibrational resonance as:

$$\chi^{(3)CARS}(\omega_{as} = \omega_2 - \omega_1 + \omega_2) = \frac{-\left(\varepsilon_0 N \big/ 6m\Omega\right)\left(\delta\alpha \big/ \delta q\right)_0^2}{\left[(\omega_2 - \omega_1) - \Omega\right] + i\gamma} \tag{24}$$

Where N is number of active molecules/atoms per unit volume, m-reduced mass, $\delta\alpha \big/ \delta q$ - Raman tensor component [8]. Dispersion for the third order nonlinearity exhibits basically the same properties as for homogenously broadened line with full width at half maximum (FWHM) equal to the doubled damping rate γ, *Figure 5* shows the real and imaginary part of $\chi^{(3)}$ vs $\left(\omega_2 - \omega_1\right)$

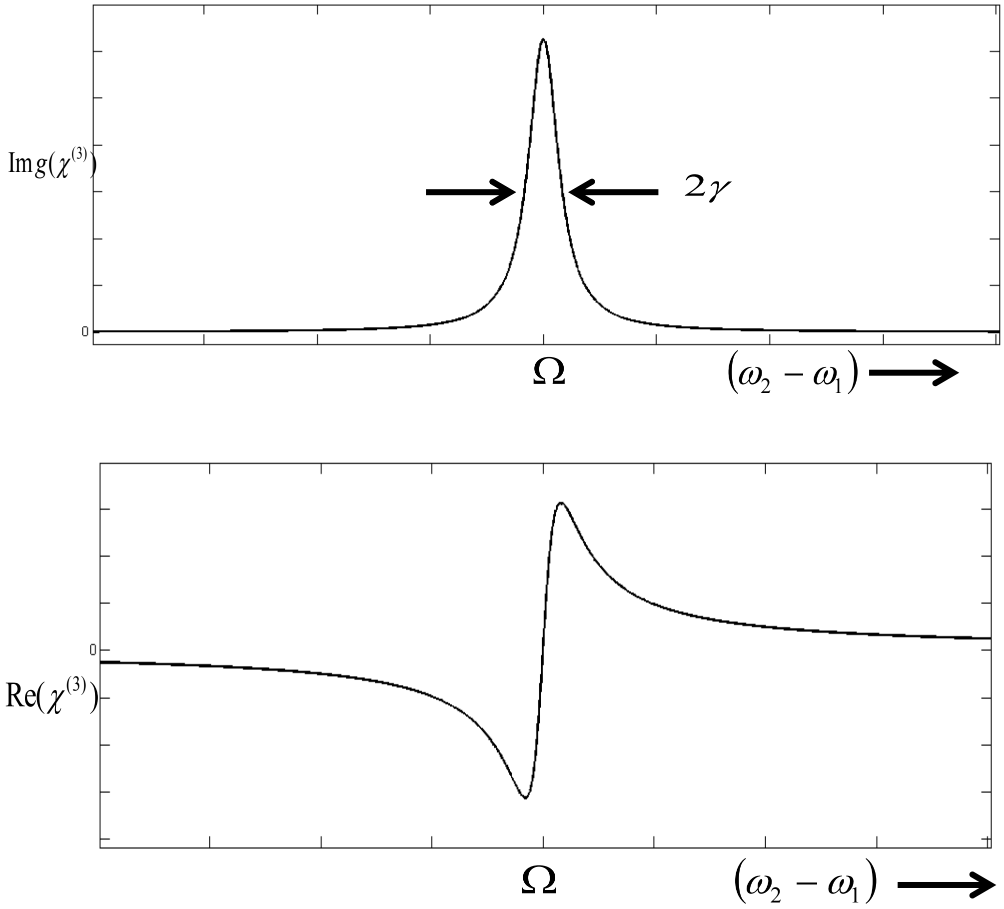

Figure 5: ***$\chi^{(3)}$ dispersion for CARS process probing Raman active vibration at Ω with the damping rate for the vibration γ***

In order to relate Raman tensor component to $\chi^{(3)}$ we briefly note that the nonlinear polarization $P^{(3)}$ can be also expressed in terms of the tensor component and vibrational coordinate q [9] for vibration at Ω

$$P^{(3)} = N \frac{\partial \alpha}{\partial q} q E \tag{25}$$

`

The polarization drives the anti-Stokes field that builds up along the beams' interaction path and can be calculated using the following wave equation that is derived from the Maxwell's equations for the electro-magnetic field:

$$\nabla^2 \vec{E}_{as} - \frac{1}{c^2}\frac{\partial^2 \vec{E}_{as}}{\partial t^2} = \mu_0 \frac{\partial^2 \vec{P}^{(3)}{}_{CARS}}{\partial t^2} \tag{26}$$

Where $\vec{E}_{as}$ is the electric field amplitude at anti-Stokes frequency of $\omega_2 - \omega_1 + \omega_3$. As was mentioned above, the four waves E_{as} E_1, E_2, and E_3 (embedded into nonlinear polarization term $P^{(3)}_{cars}$), should interact in an efficient way so that their phases match along the path. In this case the interaction yields in strong CARS signal. In order to demonstrate this we will first consider a case of degenerate CARS (i.e. $\omega_{as} = \omega_2 - \omega_1 + \omega_2 = 2\omega_2 - \omega_1$) with the three waves propagating along the same z-direction, i.e. collinear interaction. A solution to equation (26) will be sought in the following format:

$$E_{as}(z,t) = E_{as}(z)e^{-i(\omega_{as}t - k_{as}z)} \tag{27}$$

Also, we will assume that the CARS process efficiency is rather low so that (a) we can apply slowly varying (along z) amplitude approximation approach [2] and (ii) assume that fields $E_1(z)$ and $E_2(z)$ are not attenuated or depleted in the interaction process (i.e. $E_1(z) = E_1 e^{-i(\omega_1 t - k_1 z)}$, $E_2(z) = E_2 e^{-i(\omega_2 t - k_2 z)}$). This results in a condition of $\left|\frac{\partial E_{as}{}^2(z)}{\partial z^2}\right| << \left|k_{as}\frac{\partial E_{as}(z)}{\partial z}\right|$. Taking into account equation (27) and the two conditions, equation (26) transforms into a simpler, first order differential equation:

$$\frac{\partial E_{as}(z)}{\partial z} = \frac{ik_{as}}{2n_{as}}\chi^{(3)} E_1 E_2^2 e^{-i(2k_2 - k_1 - k_{as})z} \tag{28}$$

The solution for the anti-Stokes field E_{as} is straightforward for interaction length *L*. For the amplitude $E_{as}(L)$ at the medium's output we get the following:

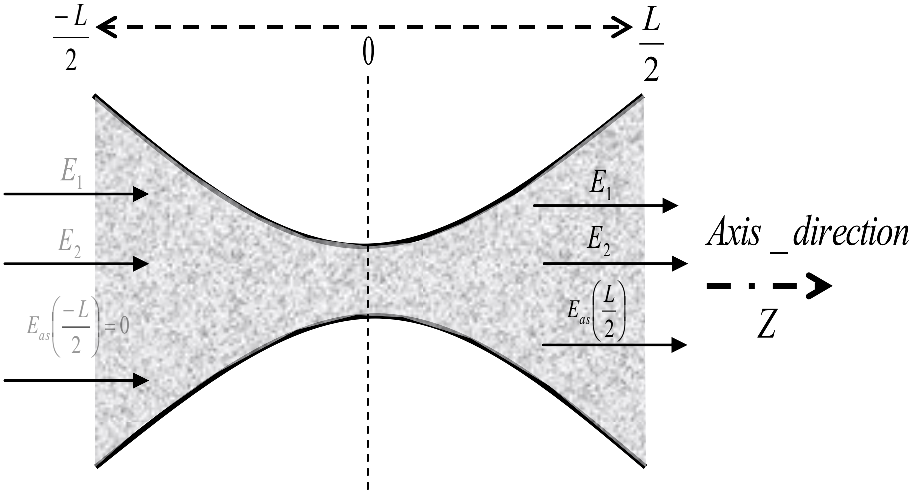

Figure 6: Focused Beams' interaction Length L

$$E_{as}(L) = \frac{ik_{as}}{2n_{as}} \chi^{(3)}_{cars} E_1 E_2^2 \left(\frac{\sin\left(\Delta k L/2\right)}{\left(\Delta k L/2\right)} \right) L \tag{29}$$

$$\Delta k = 2k_2 - k_1 - k_{as}$$

Further, assuming field-intensity relationship,

$$I_{cars} = 2cn_{as}\varepsilon_0 \left(E_{as}(L)\right)^2 \tag{30}$$

We finally get for CARS signal intensity:

$$I_{cars} = I_{cars(0)} \left| \frac{\sin\left(\Delta k L/2\right)}{\left(\Delta k L/2\right)} \right|^2 \tag{31}$$

Where $I_{CARS(0)} = \frac{k_{as}L^2}{16 n_{as} n_1 n_2^2 \varepsilon_0} \left|\chi^{(3)}\right|^2 I_1 I_2^2$

Here we used the relationships for intensities and fields (i.e. $E_1^2 = \frac{I_1}{2cn_1\varepsilon_0}$). [2]

1.5.1. Phase-matching condition.

As can be seen from the above results, I_{cars} is maximized to $I_{cars(0)}$ when $\Delta kL/2 = 0$. This condition is called a perfect phase-matching between the interacting beams.

In more details, since $L \neq 0$, the perfect phase matching requires that:

$$\begin{gathered} \Delta k = (2k_2 - k_1) - k_{as} = 0 \\ or \\ 2\frac{\omega_2}{c}n_2 - \frac{\omega_1}{c}n_1 - \frac{\omega_{as}}{c}n_{as} = 0 \end{gathered} \tag{32}$$

Where $n_{1,2,as}$ are linear refractive indices of the investigated medium at optical frequencies $\omega_{1,2,as}$. Technically, in a medium with normal dispersion the condition in equation (32) is never satisfied since $n_{as} > n_2 > n_1$. Therefore, for long enough interaction lengths (*L*), CARS signal is reduced due to the corresponding phase-mismatch factor $\left(\frac{\sin\left(\Delta kL/2\right)}{\left(\Delta kL/2\right)}\right)^2$

Figure 6 shows the results of calculations for $I_{cars}/I_{cars(0)}$ ratio when the phase-mismatch parameter Δk is varied at a fixed interaction length $L(L = 1mm)$. A solid point on the curve indicates that close to a maximum CARS signal (i.e. $I_{cars} = 0.8 \times I_{cars(0)}$) can be generated in a thin $(L = 1mm)$ layer of methanol for the corresponding near infrared wavelengths at $\lambda_1 \cong 1064nm$ ($\omega_1 \cong 1.7 \times 10^{17} Hz$), $\lambda_2 \cong 816nm$ ($\omega_2 \cong 2.2 \times 10^{15} Hz$), and $\lambda_{as} \cong 650nm$ ($\omega_{as} \cong 2.8 \times 10^{15} Hz$). For this case a broad Raman active line at $\Omega = 5.8 \times 10^{14} (i.e. \frac{\Omega}{2\pi c} \cong 2850 cm^{-1})$, corresponding to the *C=H* stretching vibration, was considered. In a solid-state material like, for example, GaAs (the same thickness $L = 1mm$) the corresponding CARS signal (open circle) is less than $I_{cars(0)}$ by more than an order of magnitude. An LO-phonon Raman active mode at 270 cm^{-1} was considered for this case.

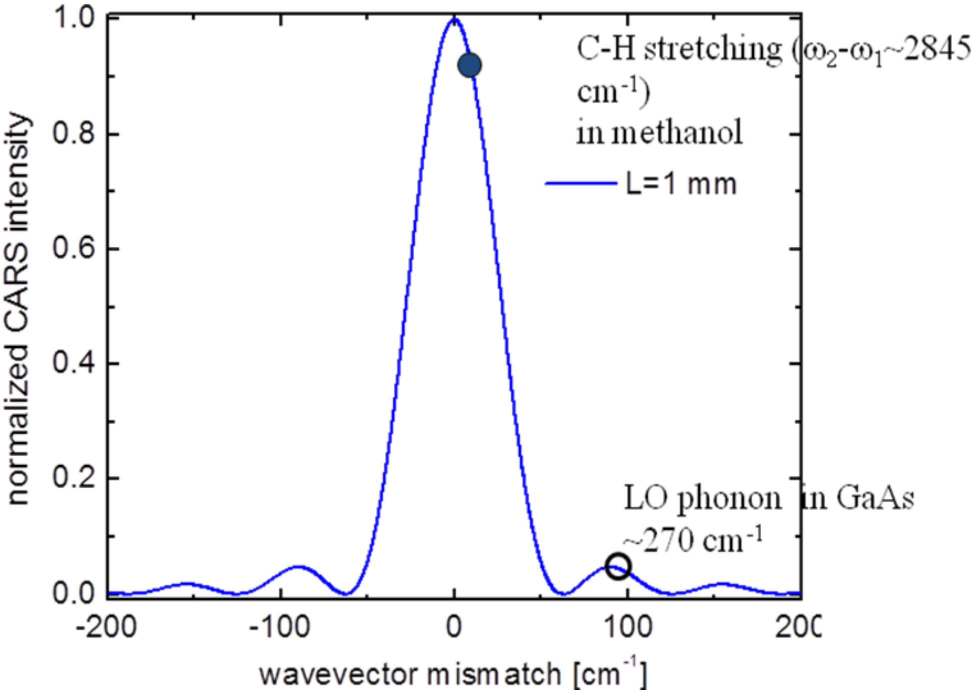

Figure 7: Phase-mismatch factor $\left(\frac{\sin\left(\Delta kL/2\right)}{\left(\Delta kL/2\right)}\right)^2$ ***for CARS signal at different phase-mismatch parameter*** Δk ***for 1 mm interaction length. Solid circle data point-CARS signal attenuation in methanol for collinearly propagating beams at*** ω_2 ***and*** ω_1***. Open circle data point-CARS signal attenuation in 1 mm long GaAs sample at the same conditions.***

In this section we considered degenerate CARS. It can be straightforwardly shown that the corresponding phase matching condition for a case of three different optical frequencies for the interacting beams at the input will result in the following phase-mismatch parameter:

$$\begin{gathered}\Delta k = k_2 - k_1 + k_3 - k_{as} = 0 \\ or \\ \frac{\omega_2}{c}n_2 - \frac{\omega_1}{c}n_1 + \frac{\omega_3}{c}n_3 - \frac{\omega_{as}}{c}n_{as} = 0\end{gathered} \tag{33}$$

We have to remind that the above phase matching conditions are valid for a collinear beam interaction. For any arbitrary beam interaction geometry (i.e. non-collinear case) a general phase matching condition needs to be satisfied. Namely, in order to achieve CARS signal maximum one needs to ensure that $\Delta\vec{k} = 0$ or

$$\Delta\vec{k} = \vec{k}_2 - \vec{k}_1 + \vec{k}_3 - \vec{k}_{as} = 0 \tag{34}$$

1.5.2. Can $\chi^{(3)}$ dispersion be measured by detecting CARS-signal versus $(\omega_2 - \omega_1)$?

We will now analyze CARS signal dependency on variation of one of the input optical frequencies (ω_1, ω_2) with a goal of finding out if dispersion data on $\chi^{(3)}$.

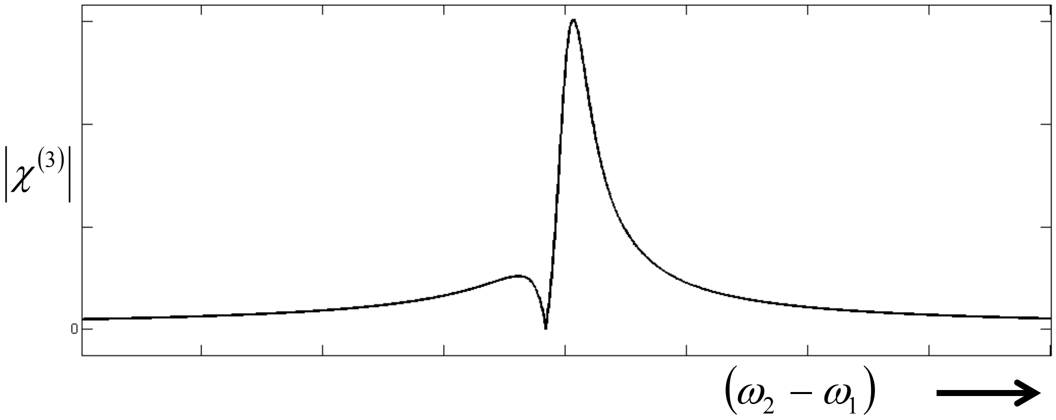

Figure 8: Normalizes $|\chi^{(3)}|$ have graphed for real and imaginary parts.

Thus, measuring CARS intensity by varying wavelength of the 'Pump' or 'Stokes' beams results in a distorted χ^3 spectrum due to the presence of non-resonant (i.e. wavelength independent) third order nonlinearity $\chi^{(3)}_{NR}$. The total detected CARS signal is shown below:

$$I_{CARS} \propto \left|\chi^{(3)}_R + \chi^{(3)}_{NR}\right|^2 = \left|\chi^{(3)}_R\right|^2 + \left|\chi^{(3)}_{NR}\right|^2 + 2\,\mathrm{Re}\left\{\chi^{(3)}_R\right\}\chi^{(3)}_{NR} \tag{35}$$

The non-resonant term can make it difficult to identify the chemically selective contributions to an image. This is especially true when imaging biological materials, as the aqueous environment gives rise to a substantial non-resonant response [9]. Various sophisticated experimental techniques have been developed to overcome the influence of the contribution due to $\chi_{NR}^{(3)}$ [10-20]. We will consider in more details the results of those works in the review section that is presented below in *chapter 2* of this thesis.

1.6. Time-Domain Coherent anti-Stokes Raman Scattering (TD-CARS).

Based on the description of CARS process provided above, the excitation and probe events in CARS process can be treated independently. Therefore, on the quantum diagram below (*Figure 9*), we will select photons from two pulses (at ω_1 and ω_2) to be used to prepare a material excitation while pulse at ω_3, that can be delayed with respect to the two, probes the result and time evolution of the excitation (*Figure 10*) as a function of time delay.

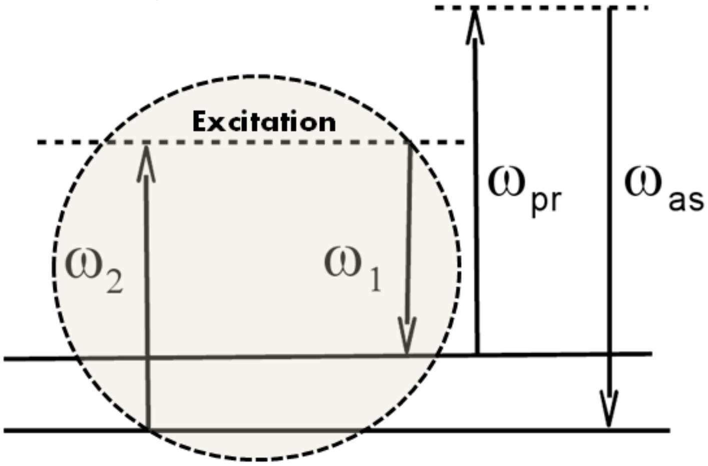

Figure 9: Quantum diagram showing Excitation from two pulses ω_1 and ω_2

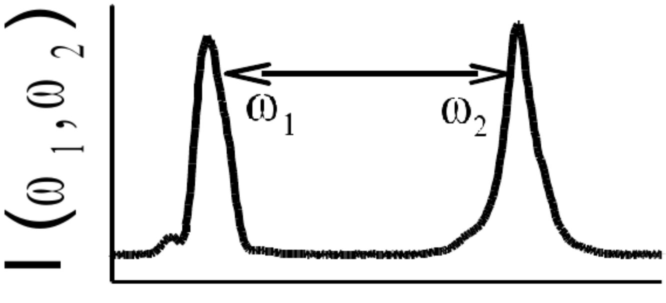

Figure 10: Time Evolution of the excitation as a function of time delay

Let us consider the case when the probe pulse (atω_3) is time-delayed with respect to the excitation pulses at frequencies ω_2 and ω_1. Excitation will result in macroscopic coherent amplitude Q. Thus, qualitatively, the approach is based on consideration that the molecular ensemble is oscillating near vibration frequency $\Omega \cong \omega_2 - \omega_1$ with time-dependent coherent amplitude$Q(t)$.[10]

$$Q = \frac{1}{N}\sum_{i=1}^{N} q_i \tag{36}$$

Where q_i are normal displacement coordinates of the individual molecular vibrations at Raman frequencyΩ within the volume of excitation. The first two pulses act as an excitation force to phase-in all the individual vibrations thus creating a macroscopic amplitude $Q(t=0) = Q_{\max}$ since all the individual phases at q_i have the same fixed value determined by the phase of the excitation pulses. After the pulses are gone, the macroscopic amplitude $Q(t>0)$ starts to decay freely due to de-phasing of the individual vibrations. This is in direct analogy with a free-induction decay effect well characterized for direct atomic transitions [11]. However, for the case of CARS, we can talk about the decay of the induced third-order polarization described by equation (25) in the previous section. Various de-phasing processes are caused by intra- and inter- molecular interactions (e.g. elastic collisions and free translational motion in gases, enharmonic potential in solids, etc.). The following set of equations provides anti-Stokes pulse signal intensity versus time delay (td) of the probe pulse $E_3(t)$ with respect to the excitation pair from the molecular ensemble of density$N$:

$$\begin{aligned}
&S_{as}(t_d) \propto \int_{-\infty}^{\infty} \left|E_{as}(t)\right|^2 dt \\
&\frac{\partial E_{as}(z,t)}{\partial z} = k_{as} E_3(t-t_d) Q(z,t) \\
&Q(t) = \frac{1}{N}\sum_{i=1}^{N} q_i(t) \\
&\frac{\partial q_i}{\partial t} + (\gamma_i + i\gamma_x) q_i = k_q E_1(t) E_2^*(t)
\end{aligned} \tag{37}$$

`

In the equations, constants k_{as} and k_q for the excitation pair and the probe pulses represent the respective field coupling to the molecular system and are both proportional to the Raman cross-section (σ) of the vibration. The Raman cross-section can be directly measured in spontaneous Raman scattering experiment by a virtue of expression:

$$I_{Sp} = N\sigma I_L L\Delta\Omega \tag{38}$$

Where, I_{Sp}-spontaneous Raman signal intensity, N stands for molecular density, I_L-laser intensity, L interaction length, $\Delta\Omega$-solid angle of acceptance of detector.

Technically, the individual amplitude q_i is a complex function and thus can be characterized by their amplitude and phase parts. The individual amplitude can be affected by internal (intra-molecular) interactions with other molecular or lattice degrees of freedom with a characteristic rate γ_i that is uniform for each molecule. The phase term is rather impacted by external (intermolecular) interactions with surrounding bath by means of collisions and velocity drifts that both result in random phase shifts for the vibration and can be characterized with $\gamma_x - rate$. With Q representing ensemble average, its time-varying solution is, in general, a complex function that takes into account various amplitude and phase relaxation processes. In many cases though ensemble averaging in time domain yields in phase correlations that leaves $Q(t)$ to be a real function [12].

As a simplest case, let us consider a homogenously broadened Raman active line with width of 2γ. Let us also assume that the polarizability tensor has only isotropic component (i.e. linearly polarized laser light scatters into linearly polarized (the same as the incident) light at Stokes shifted frequency. Time-dependent electric field amplitudes for all the laser beams are real and the electric fields are represented as discussed above in equations (1, 9). Assuming also that vibration energy Ω is large enough so that $\hbar\Omega >> k_B T$ (e.g. $\hbar\Omega > 3k_B T$) and there is no linear absorption or depletion of light along propagation (*z*) direction. Thus, Q is only function of time and equation for the coherent amplitude can be derived from the master set equations in the following form:

`

$$\frac{dQ(t)}{dt}+\frac{Q(t)}{T_2}=\kappa_{12}E_1(t)E_2(t)$$
$$\kappa_{12}=\sqrt{\frac{3\sigma c\Omega_R}{16\hbar}}\frac{m_R}{(\omega_1-\omega_2)(\omega_1-\Omega_R)^2}; \tag{39}$$

Where, T_2 – de-phasing time ($T_2=1/\gamma$), σ –Raman (differential) cross-section [m^2/sr], m_R –reduced molecular mass.

Thus, time-delayed anti-Stokes field amplitude can be expressed as follows:

$$\frac{\partial E_{as}(z,t)}{\partial z}=\kappa_{as}E_{pr}(t-t_d)Q(t)e^{i\Delta kz};\ E_{as}(0,t)=0$$

$$E_{as}(L,t)=\kappa_{as}E_{pr}(t-t_d)Q(t)Le^{-i\Delta kL/2}\left(\frac{\sin\frac{\Delta kL}{2}}{\frac{\Delta kL}{2}}\right)$$
$$\kappa_{as}=\frac{N\pi}{ck_{as}}\left(\frac{\omega_{as}m_R}{\omega_{pr}-\Omega_R}\right)^2\sqrt{\frac{3\sigma\Omega_R}{c\hbar}} \tag{40}$$

$$\Delta k=k_{as}-k_{pr}-(k_1-k_2)$$

Here, t_d - delay time, L-interaction/sample length, N-molecular/ion density [1/m^3]. Here we assumed that the pulse at ω_3 is used as a probe pulse with the electric field amplitude $E_3=E_{pr}$ (also $\omega_3=\omega_{pr}$, and $k_3=k_{pr}$).

Now, equation (36) can be solved to yield in $Q(t)$:

`

$$Q(t) = \frac{4\pi\kappa_2}{c\sqrt{n_1 n_2}} e^{-\frac{t}{T_2}} \int_{-\infty}^{t} \sqrt{I_1(t')I_2(t')} e^{\frac{t'}{T_2}} dt'$$
$$Q(t \to -\infty) = 0$$
$$Q(t) = \frac{4\pi\kappa_2}{c\sqrt{n_1 n_2}} e^{-\frac{t}{T_2}} f_{ex}(t) \tag{41}$$
$$f_{ex}(t) = \int_{-\infty}^{t} \sqrt{I_1(t')I_2(t')} e^{\frac{t'}{T_2}} dt'$$

Solution for time-domain CARS energy density/signal (*S(t_d)*)

Since the anti-Stokes signal is related to the corresponding field by**:**

$$S(t_d) = \frac{cn_{as}}{4\pi} \int_{-\infty}^{\infty} \left| E_{as}(L,t) \right|^2 dt \tag{42}$$

We finally obtain

$$S(t_d) = S(0) \int_{-\infty}^{\infty} e^{\frac{-2t}{T_2}} \varepsilon_{ex}^2(t) \varepsilon_{pr}(t - t_d) dt \tag{43}$$

$$S(0) = \left(\frac{4\pi\kappa_{12}\kappa_{as}}{c^2} \right)^2 \frac{I_{10} I_{20} I_{pr}}{n_1 n_2 n_{pr}} n_{as} L^2 \left(\frac{\sin \frac{\Delta k L}{2}}{\frac{\Delta k L}{2}} \right)^2 \tag{44}$$
$$\varepsilon_{ex}(t) = \int_{-\infty}^{t} \varepsilon_1^{1/2}(t') \varepsilon_2^{1/2}(t') e^{\frac{t'}{T_2}} dt'$$

$\varepsilon_{1,2,pr}(t)$ are excitation and probe pulse intensity envelopes.

Below examples of the coherent amplitude $Q(t)$ calculations for the case of two different de-phasing times T_2.

`

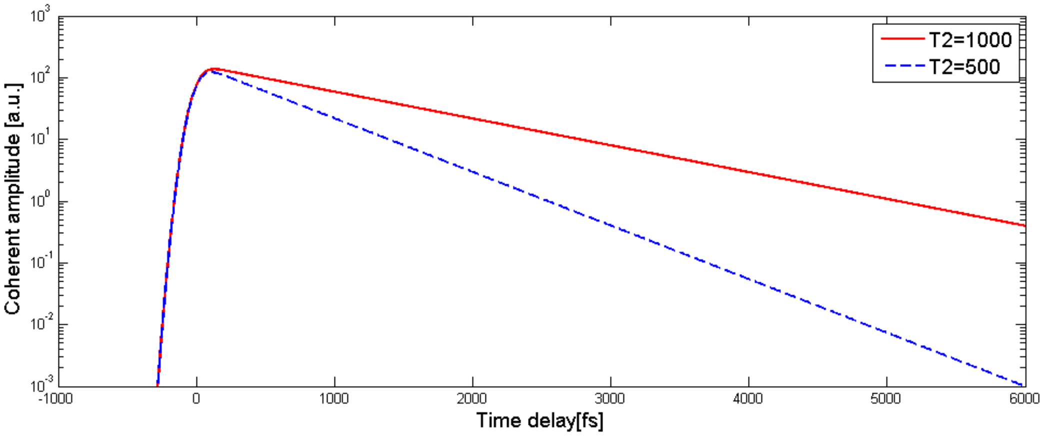

Figure 11: Time evolution of the coherent amplitude $Q(t)$ *after ultra-short pulse excitation* $(t_p << T_2)$ *for two different de-phasing times* $T_2 = 500\,fs$ *('dashed curve') and* $T_2 = 1\,ps$ *('solid curve').*

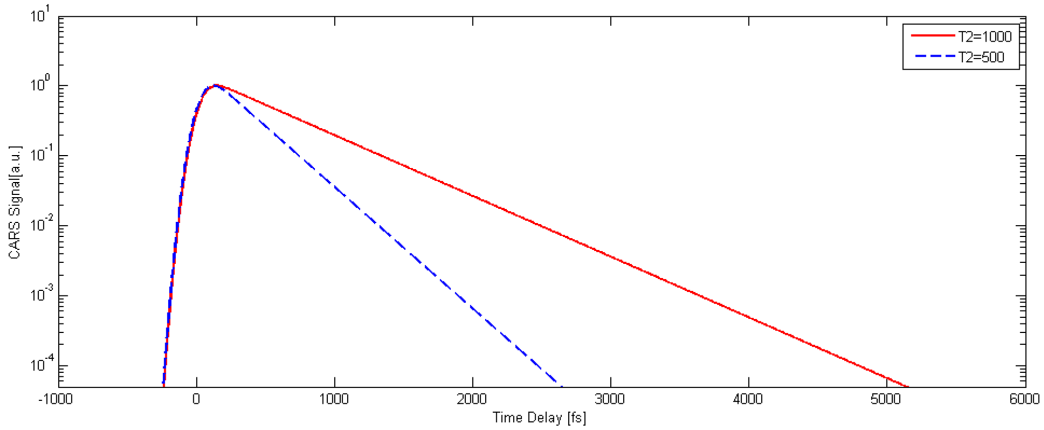

Figure 12: Time-domain CARS signal intensity for the above solutions for $Q(t)$ *simply calculated using equations (43) and (44).*

1.7 Objective of the thesis

The primary objective of the thesis is to outline state-of-the art for CARS spectroscopy and microscopy and their applications in biomedical imaging and condensed matter characterization. Namely, the goal is to apply the technique to characterize soft- (including biological media) and traditional condensed matter. I will present recent works on CARS that relate to applications of CARS technique in imaging of biological media. I will also present technical approaches as concerned experimental realization of CARS. I will present our experimental approach in particular details and discuss problems and issues related to wavelength tunable femtosecond

`

pulse generation using optical parametric oscillation. And lastly, I will demonstrate the results of our recent experiments on time-domain femtosecond CARS with regard to its applications on tracing phonon dynamics in solid state and imaging of biological cells and tissue.

Chapter 2

Literature Review

2.1. Motivation for new developments and history of CARS.

Investigation of molecular properties in complex systems and determining the spatial distribution of specific molecular species to cellular and sub-cellular scale has been of prime focus in the fields of biology and applied microscopy. Developments in various natural and artificial fluorescent probes made chemically selective imaging feasible. But these techniques are bound to certain materials and require detailed preparation and introduce foreign agents into the sample which sometimes lead to photo bleaching problem. For chemical species and cellular components that are insensitive to fluoresce or cannot support labeling excellent contrariety among distinct chemical species can be obtained by using infrared radiation tuned to characteristic vibrational frequencies, but the spatial resolution, limited to few micrometers because of the long wavelength of light used and IR absorption of water hinders its application to live cell and aqueous medium. Infrared microscopy is generally insufficient to resolve cells or smaller structures.

High resolution microscopy of biological samples has been demonstrated with Raman scattering microscope [13]. Raman scattering microscopy is extremely useful as it occurs for any wavelength of light. But, On the other hand Raman scattering requires high average powers because of small cross section of Raman scattering and require several hours to acquire Raman images of cells and tissues. Such long exposure time limits the application of Raman microscopy to study of dynamic living systems. A multi-photon Microscopy based on coherent anti-Stokes Raman scattering (CARS) [14] was put forward as an alternative way of providing vibrational contrast.

2.2. Literature Survey.

2.2.1. Discovery and early original works on CARS.

In 1964 P.D. Maker and R. W. Terhune at scientific laboratory of Ford Motor Company conducted a series of experiments to study nonlinear optical effects of the third order due to induced polarization by the electrical field strength [15]. A giant pulsed ruby laser was used in this study as the pump source and a wide range of crystalline and isotropic material are studied.

This study included optical third harmonic generation, electrical field induced second harmonic generation, resonant and non resonant mixing of waves at three different frequencies, intensity dependent changes in the complex index of refraction and Raman laser action.

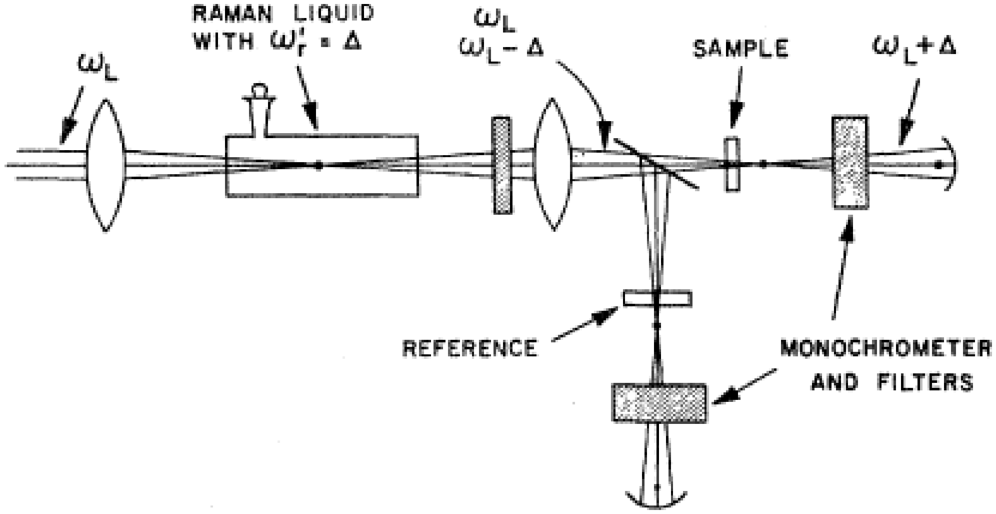

Figure 13: Three wave mixing experiment [15]

Parameter	Pump Laser	Stokes laser	Probe laser
Laser description	Ruby laser	Cell Filled Benzene	
Wavelengths tuning	(ω)	(ω)-Δ	(ω)-2Δ
Frequencies	50KW	10KW	50W
Repetition rates	<10 photon/pulse	_	_

Table 1: Experimental specifications of P D Maker et al. [15]

Ruby laser of frequency $\omega_2$is passed through a Raman shift (Raman Liquid) to create a second harmonic beam at frequency$(\omega_L - \Delta), \omega_L$ and then these two beams are focused onto the sample. The pulses generated from both the beams are over lapped in space and time and resulting frequency $(\omega_L + \Delta)$ was observed .Benzene was used as the generator liquid for this experimental setup. This "*Three Wave Mixing Experiments*" was termed as Coherent Anti Stokes Raman Scattering (CARS) by Begley et al. at[16] Stanford University in 1974. Since then a numerous applications of CARS spectroscopy were successfully demonstrated. The research spanned across many fields in physics[1, 2, 17], biology and medicine [5, 18].

2.2.2. CARS Microscopy

The first realization of CARS-microscopy dates back to the original work by Duncan et al.[19]. The CARS technique was implemented in degenerate two-color modes where two independently tunable synchronously pumped dye lasers provided intense ps duration laser pulses in 565-620 *nm* and 620-700 *nm* spectral ranges. Images of onion-skin cells have been obtained with 0.7 μm spatial resolution by using the CARS signal produced by the 2450 cm^{-1} band of deuterated water.

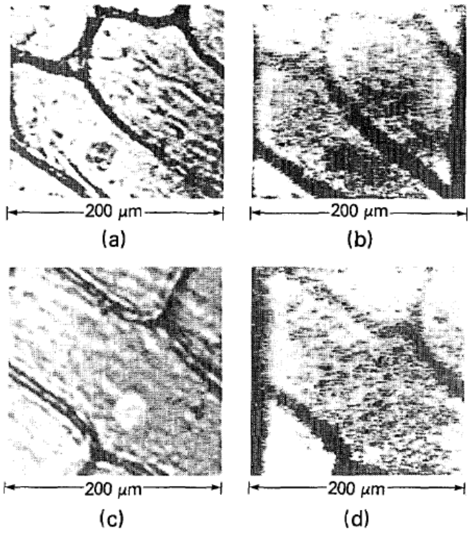

Figure 14: CARS Image of D2O soaked Onion slices. [19]

The dye lasers have been pumped by a mode-locked argon ion pumped laser and thus the laser part of the set up consisted of 3 open resonator laser sources. Beams are spatially separated to satisfy phase matching requirements. After interaction in the sample, both input beams and the generated anti stokes beams are collected by a conventional microscope. The experimental arrangement used in their research is shown below in *Figure 15*.

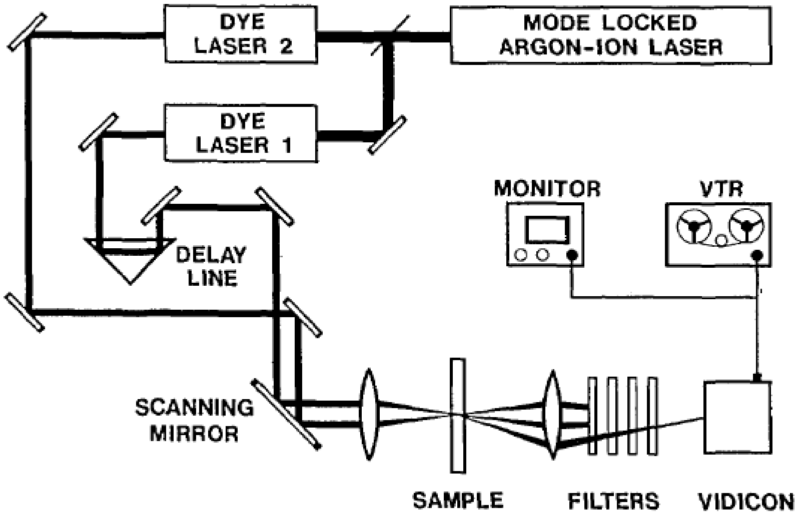

Figure 15: Experimental setup of Duncan et al. [19]

However the non collinear beam geometry used in the work limited the image quality and excitation with visible wavelengths resulted in a large non resonant background. Though CARS-microscopy has lot of advantages over conventional microscopic techniques, it has its own disadvantages. CARS microscopy is not background free [14, 20]. Also, intrinsically weak induced nonlinear polarizability requires sophisticated laser excitation sources with high peak power.

2.2.3. Recent advances in CARS microscopy.

The interest to CARS microscopy was renewed quite recently after Zumbush et al. [14] reported CARS microscopy experiments in the spectral region around 3000 cm^{-1} with high spatial resolution (<400 *nm*) and three-dimensional sectioning capability. The authors employed a Ti:Sapphire based chirped- pulse amplified(~1.2 μm) system at a *kHz* repetition rate that pumps a tunable optical parametric amplifier system. Thus, two independently tunable ultrashort pulses (in the vicinity of 850 *nm* and 1200 *nm*) can be used to implement two-color CARS. The CARS microscopy experiment required only a moderate average power for excitation (0.1mW) which is tolerable by most biological samples.

`

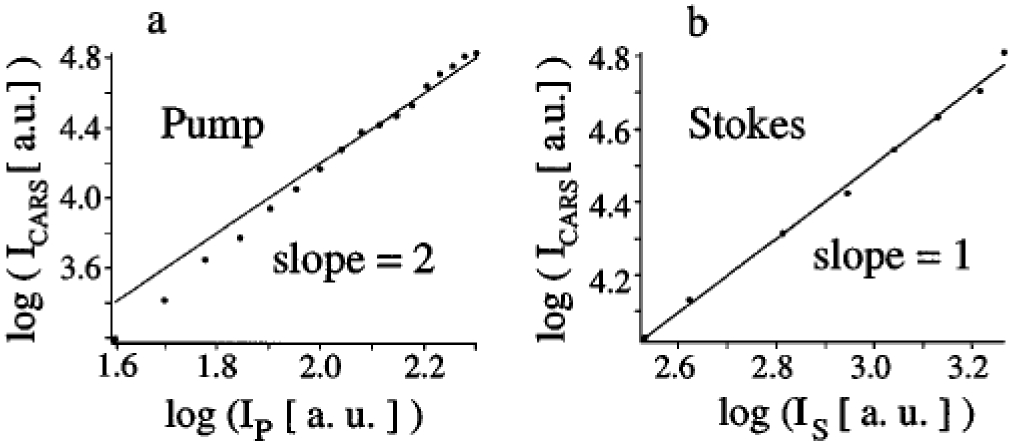

Figure 16: Graphs of dependence of CARS Signal on the excitation powers of pump and stokes beams.[14]

A high NA objective lens was used in this experiment in order to focus the beams tightly thus resulting in large cone angle for the wave-vectors which, in turn, relaxed the phase matching condition. Because of the nonlinear intensity dependence, the CARS signal is only generated within a small volume (about $0.5 \times 10^{-15} L$) at the focus thus allowing three-dimensional sectioning of relatively thick samples. This system suffers from higher level of complexity as it involves at least two pump lasers, CPA, and regenerative and parametric amplifier optics.

A similar approach was used in a subsequent work by Hashimoto et al.[21] However, to facilitate spectral selectivity and to be capable to obtain CARS spectra, the authors used a picoseconds laser to satisfy a condition of having high enough peak intensity and narrow spectral bandwidth for the pulses. The pulse duration of the Ti:Sapphire based regeneration amplifier output was extended to 2.0 *ps* by applying a picoseconds mask, which was placed in the pulse stretcher of the CPA system to reduce the spectral bandwidth. The typical spectral bandwidths of the ω_1 and ω_2 beams were 14.5 cm^{-1} (0.85 *nm*) at 12883.5 cm^{-1} (776.19 *nm*) and 21.5 cm^{-1} (1.45 *nm*) at 11882 cm^{-1} (841.61 *nm*), respectively. Again, the system has an even higher level of complexity than the one described in the work by Zumbush et al. [14]and both are prone to various kinds of pulse parameter instabilities. The *multi-kHz* CPA system approach was replaced by the systems employing mode-locked *fs/ps* Ti:Sapphire based oscillators operating at 80-100 *MHz* repetition rates. High NA objective lens and an effectively higher rate of the anti-Stokes photon detection have made possible of obtaining high contrast images of biological media.

These works by Zumbush et al. [14] and Hashimoto et al. [21]triggered interest within several research groups which took the CARS microscopy to the next level. A drawback of this work is use of broadband femtosecond pulses that are not optimal for vibrational spectroscopy from several aspects.

Ji-Xin Cheng et al. [20] reported on CARS-microscope with two synchronous 80*MHz* picoseconds pulse trains generated from Ti:Sapphire laser. Lock-to-clock system was used in synchronizing the 80*MHz* pulse trains. The time delay between system also allows in electronically adjusting the time delay between the two pulses with wavelength tuning range from 700 *nm* to 950 *nm*. Thus, the frequency difference between the two beams can cover almost an entire spectrum of molecular vibrations (e.g. 100-3700 cm^{-1}). The approach used in this work also features detection of CARS signal propagating in the direction back with respect to the incoming laser beams allowing significant reduction in non-resonant (background) signal (see *Figure 17*). The technique was given an abbreviation of Epi-CARS.

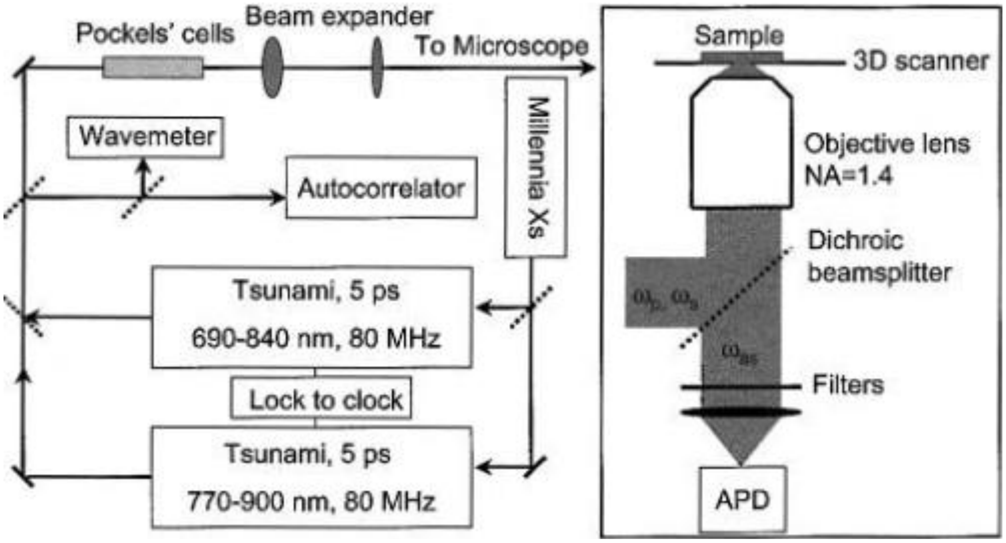

Figure 17: Schematic diagram of synchronized Pico second laser system and the epi-detected CARS (Epi-CARS) Microscope.[20]

`

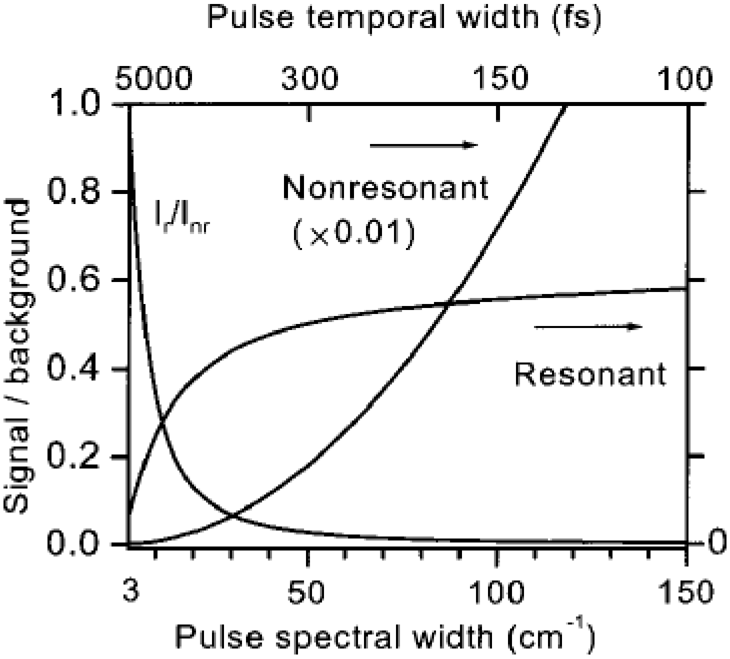

Figure 18: Intensity of resonant and non resonant signals as a function of spectral width.[20]

The combination of near infrared picoseconds pulse train and the Epi-detection geometry allows CARS Imaging of living cells in the whole spectral region of molecular vibration. This experiment offers higher spectral region of molecular vibration .This experiment offers higher spectral resolution and sensitivity than the previous femtosecond experiment. The evident advantage of this backward or Epi detection is the efficient suppression of the non-resonant signal from the bulk (Volkmer et. al.).[22]

As was mentioned above, detection of CARS in backward direction (Epi-CARS technique) suppresses efficiently the solvent background and increases significantly the sensitivity of CARS microscopy in detecting molecular groups with specific vibration frequency.

`

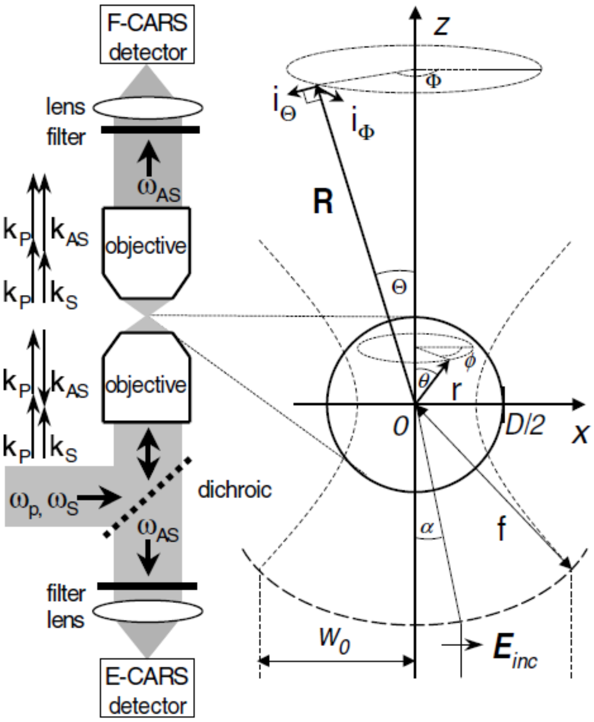

Figure 19: Experimental setup of Volkmer et al. for F-CARS and E-CARS along with parameters used in calculations.[22]

Detailed calculations and comparisons of the Epi-CARS versus conventional forward CARS (F-CARS) methods are presented in the work of Volkmer et al.[22] Briefly, in the study, interaction of Gaussian beams of '*Pump*' and '*Stokes*' light pulses with beams waist of w_0 that are focused by a high NA objective were considered to generate CARS signal from a spherical sample of a diameter D. The radiation field of induced polarization, $P^{(3)}(r,\omega_{as})$ is integrated over the sample's volume and the detected in the forward (F) and backward (Epi) directions. The ratio for the two signals versus the diameter D is shown on the *Figure 20*.

`

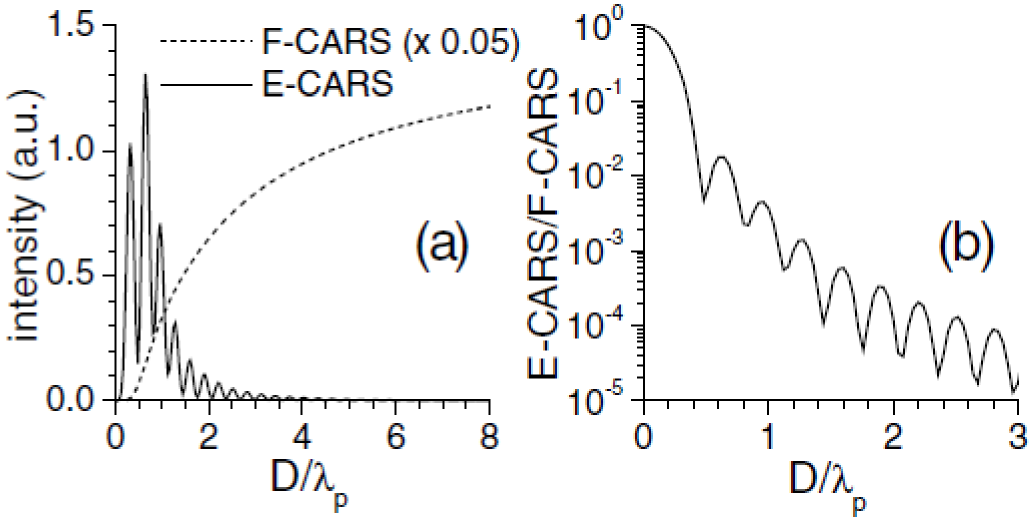

Figure 20: Graphs of F-CARS and E-CARS.[22]

one can see that E-CARS can be used as an effective way to enhance image contrast due to its ability to suppress the nonresonant background from a surrounding medium. It has been observed through this experiment that E-CARS microscopy dramatically increases the sensitivity of CARS detected for scatterers smaller than the wavelength of light. The first deep tissue imaging CARS experiment with signal collected in the *Epi* direction showed an increased contrast for larger structures as well as was reported by Evans et al.[23] In a different highlight, a first step towards CARS endoscopy has been demonstrated by F.Legare et al in 2006 [24]. In this experiment authors used excitation pulses delivered by an optical fiber. The generated CARS signal was detected in Epi-mode and the signal was collected by the same fiber. Authors demonstrated images of 5 *micron* diameter polystyrene beads and reported a spatial resolution of few microns.

In the work published by Potma et al.[25] optimized peak powers help to boost the nonlinear signal. Laser pulse widths of 1–2 *ps* have been found to match to the typical vibration bandwidths to optimize the CARS signal, with minimized non-resonant background while maintaining fairly good spectral resolution. Two independently tunable picoseconds Ti:Sapphire lasers have been electronically synchronized with jitter time as small as 20 *fs* to provide ω_1 and ω_2 beams at corresponding wavelengths of 850 *nm* and 750 *nm* respectively. Authors reported improvement in signal-to- noise ratio and demonstrated an image of a mouse cell at a 1570 cm^{-1} Raman shift.

`

2.3. Laser sources for CARS Microscopy.

Kee et al. reported further progress [26] in developing a Ti:Sapphire based CARS microscopy laser system that would utilize a single *fs* pulse oscillator source. Through pulse spectral filtering and broadband continuum generation in an optical fiber, the system was capable of delivering broadband CARS imaging capability along with fast CARS spectra acquisition. Vibrational spectra over a bandwidth of 2500 cm^{-1} with a resolution of 13 cm^{-1} have been demonstrated. However, apart from employing a free space optics resonator and components, the drawback of the system is in substantially reduced spectral brightness/power of one of the pulses and certain complexity in generating and tracking parameters of the spectrally filtered and continuum pulses.

The Ti:Sapphire based master oscillator source was used by Andresen et al. [27]to demonstrate a photonic crystal fiber (PCF)-based light source for generating tunable excitation pulses that are applicable to coherent anti-Stokes Raman scattering (CARS) microspectroscopy. The CARS pump pulse was generated by spectral compression of a laser pulse in a PCF. The Stokes pulse was generated by red shifting a laser pulse in a PCF through the soliton self-frequency shift. This setup allowed for probing of Raman lines of up to 4000 cm^{-1} shift with a spectral resolution of approximately 25 cm^{-1}. Another effort was reported recently by the same group [28] where specially designed mode-locked Yb-doped fiber laser served as a master source.

Yakovlev et al. [29] reported a version of the CARS set up based on a Nd:Vanadate ps laser for imaging applications and microspectroscopy. High energy, *ps* Nd:Vanadate laser pulses generated a *ps* continuum in nonlinear fiber providing tunable output. The designed set up allowed accessing Raman vibrations in the range of 700-1700 cm^{-1}. Apart from rather low peak intensities and average power, another main disadvantage of the source based on nonlinear interactions in fiber is in the fact that the master laser pulse intensity fluctuations are tripled due to the corresponding third order nonlinear interaction.

And lastly, an approach based on the dual wavelength picosecond optical parametric oscillator source was reported recently by Ganikhanov et al [30]. The signal and idler beams from a picosecond, synchronously pumped optical parametric oscillator (OPO) provided the two colors necessary for CARS microscopy. The OPO is continuously tunable with the frequency

`

difference between the two beams being over a broad range of Raman shifts 100–3700 cm^{-1}. The broad wavelength tuning range and the corresponding access to Raman bands have been achieved by varying the temperature of a single nonlinear crystal. Apart from that fact, the near-infrared output at 900–1300 *nm* allowed for deep penetration into thick samples and reduced nonlinear photo damage. Applications of this light source to in vivo cell and ex vivo tissue imaging are demonstrated.

`

Chapter 3

Experimental Setup

This chapter discusses the experimental setup for nonlinear optical spectroscopy and imaging of the biological media. This chapter is broken down into four sections. The basic layout of the optical system is described first, followed by the detailed layout for OPOs, and finally the imaging, automation control, and data acquisition are explained.

The Department of Physics and Robert Byrd Biomedical Research center at West Virginia University (WVU) has developed Ultrafast Optics laboratories (UFO-labs) under the guidance of Dr. Feruz Ganikhanov. The mission is to develop background free high resolution imaging and spectroscopy technique. In order to enable Coherent Anti-stokes Raman Scattering (CARS), Second Harmonics Generation (SHG), Third Harmonics Generation (THG), and Sum Frequency Generation(SFG) techniques, near-IR femtosecond Optical Parametric Oscillators (OPOs) that allows tunablity of lasers to different wavelengths and frequencies, were developed. All these nonlinear microscopic techniques were used for characterizing biological media and soft condensed matter. As was mentioned above, this thesis focuses on different aspects of realization of CARS spectroscopy and microscopy.

3.1. The general optical table layout

A picture of experimental set up followed by the layout are presented below. As shown in *Figure 21*, our setup consists of a pump laser, continuous wave 780 *nm* (Coherent Verdi V-18), that pumps Ti:Sapphire Laser (Mira-HP). The output from this high power mode-locked Ti:Sapphire laser delivering pulses of 95-115 *fs* and 76 *MHz* repetition rate is passed through an isolator and then after some dispersion pre-compensation the laser beam passes through Glan-Taylor prisms where it splits into two laser into vertical polarization and horizontal polarization. This light can be computer controlled in less than 10 mW increments, using a rotation stage stepper motor with half-wave plate aligned in series with a Glan-Taylor prism, up to the maximum available output power of 3.5W. The horizontal beam (parallel to optical table) is split into two separate beams using a beam splitter.

`

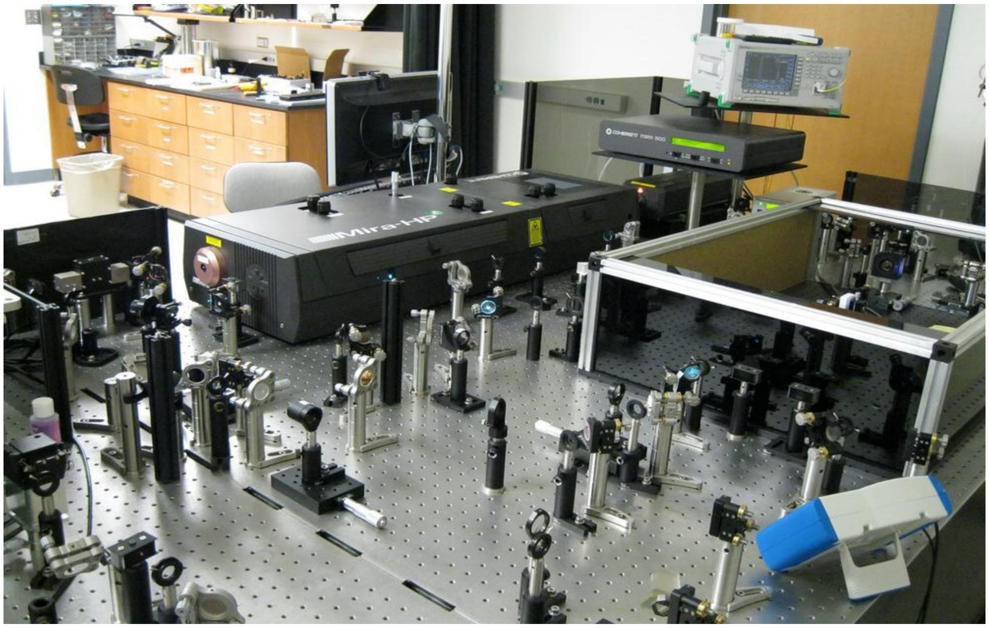

Figure 21: Picture of the setup for CARS with Coherent Verdi (on the far left corner of the table) pumping Ti:Sapphire Laser (Mira-HP), two custom built OPOs on the right side of the table, and mirrors, lens, and telescopes for guiding the beam to the microscope.

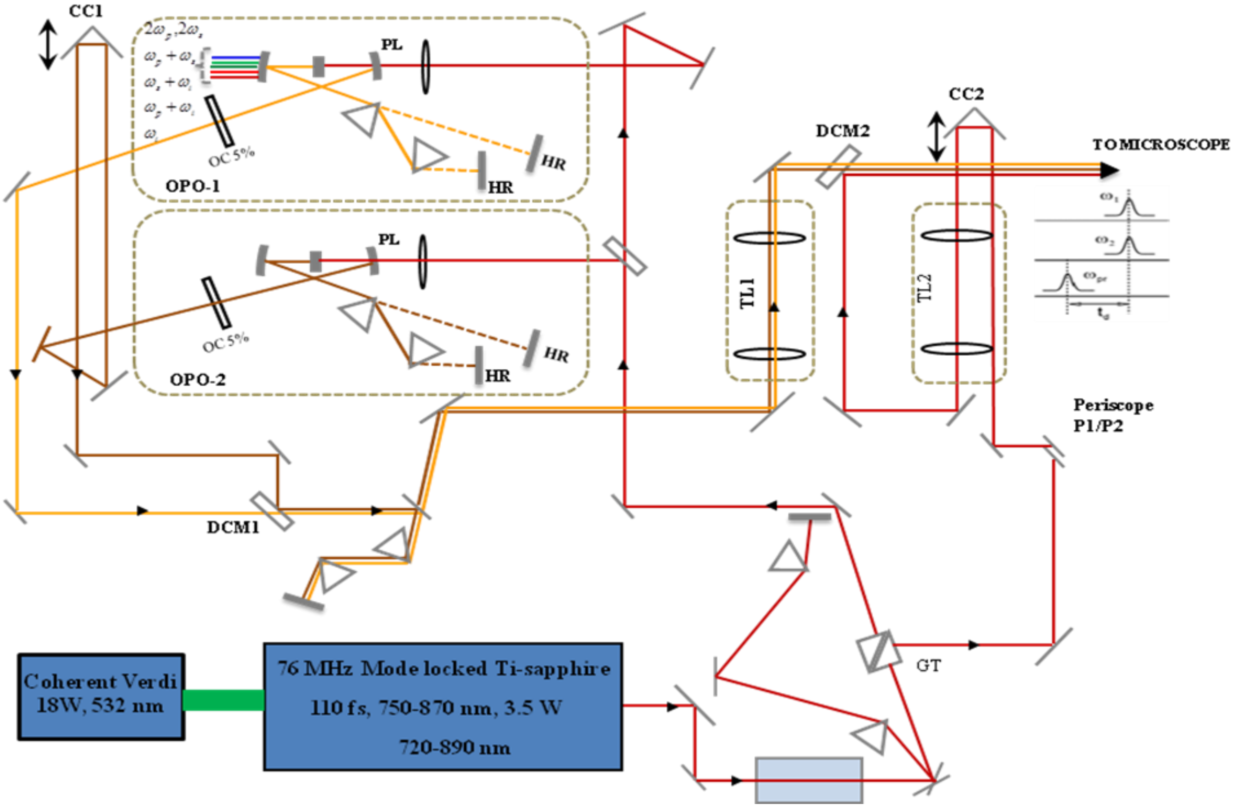

Figure 22: Schematic of the experimental set up. Time-domain CARS process involved two OPO pulses at tunable ω_1 and ω_2 optical frequencies used to coherently excite Raman active vibrations while a delayed replica of Ti:Sapphire pulse at ω_{pr}

`

These two beams synchronously pump the two Optical Parametric Oscillators(OPOs) and the vertical component of the Ti:Sapphire output is converted into horizontal polarization using a periscope. The OPOs can be independently tuned across near infrared (IR) wavelength range. Details on the OPO performance and characteristics can be found below [31]. The output from the two OPOs at frequencies ω_1 and ω_2 are properly synchronized in time and space by guiding the output from one the OPOs into a corner cube (CC1 as mentioned in *Figure 22*) placed on a translation stage. The translation stage allows the a proper time delay so the output from the two OPO's matches in time and space. These two beams then pass through a set of dichoric mirrors, prisms and telescope before they meets the third beams which was converted into horizontal polarization by a periscope. Proper time delay between these beams with the third beams at frequency $\omega_3(\omega_{pr})$ is maintained my using the corner cube(CC2, see *Figure 22*). So at the end we have three ultrashort laser pulses which are the sources for optical imaging and ultrafast spectroscopy.

3.2. Optical parametric oscillators

As shown in *Figure 23*, the OPO cavity is formed by two concave high reflectors HR1 and HR2, a plane HR3 mirror, and a 5%-10% output coupler (OC). All HR mirrors are rated at >99.3% reflection. Pump beam is focused through a high reflecting concave mirror HR2 and then into the PPSLT crystal using a lens (L1). Through the course of investigation concave mirrors with two distinct radii of curvature (*r*=100 *mm* and 200 *mm*) were employed. Correspondingly, the lens focal length is chosen to provide an optimal match of the pump and oscillating signal beam spot sizes in the crystal. In order to change the cavity roundtrip time an output coupler is mounted on a precision translation stage.

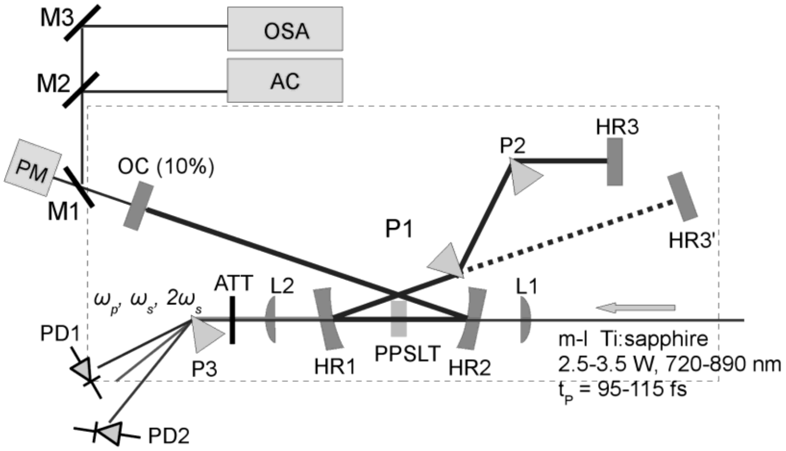

Figure 23: The experimental set up. HR1, HR2- high reflection coated mirrors with either 10 or 20 cm radius of curvature. PPSLT- 1 mm long multigrating period periodically poled stoichiometric lithium tantalate crystal. P1, P2, P3- SF10 glass material Brewster angle cut dispersive prisms. HR3, HR3'- flat surface, highly reflecting mirrors. OC- OPO output coupler with 5-10% transmission. L1, L2- plano-convex lenses. ATT - light power attenuators. PD1, PD2 - calibrated photodiodes. AC - intensity autocorrelator. OSA- optical spectrum analyzer. PM- power meter. M1, M2, M3- beam steering flip-mirrors. The pump beam is the output of the high-power Ti:Sapphire oscillator. The OPO resonator optics favored signal wave to resonate. ω_p, ω_s, $2\omega_s$ ***are optical frequencies for pump, signal, second harmonic of the signal wave respectively.***

The OPO could be operated with or without a Brewster angle cut prism pair, P1 and P2, used for the intracavity dispersion compensation. The OPO was investigated in its signal branch using four mirror sets with maximum reflections at 940, 1100, 1200 and 1300 *nm*. The PPSLT crystal (Deltronic Crystal Industries, Inc.) is 1 *mm* long, 0.5 *mm* in width and 15 *mm* high with thirteen poling periods ranging from 17.60 *μm* to 24.80 *μm* distributed along the crystal height in 1 *mm* sections at 0.6 *μm* intervals. The crystal is AR coated for the 950-1250 *nm* wavelength range with less than 2% in residual reflection in the 750-850 *nm* range. A copper holder enclosing the crystal on two sides was constructed with temperature control accurate to within 1°*C*. The OPO output was analyzed using a broadband intensity autocorrelator, fast InGaAs photodiodes, optical spectrum analyzer (Anritsu M9710), a wavelength sensitive average power meter, and 1.2 *GHz* input bandwidth oscilloscope (LeCroy 104*MXs*, 5 *GS/s*). The photodiodes were power and wavelength calibrated so that the multi-color power output transmitted through mirror HR1 could be estimated with good precision at the pump wavelength and each wavelength generated within the crystal. The OPO cavity stability range (for a given signal wavelength and various cavity lengths) and the pump and signal spot sizes in the crystal were calculated numerically. The precise positions of the concave cavity mirrors and the crystal were controlled by micrometers.

3.3. Imaging setup.

Three ultrashort laser pulses, two created by the OPOs and one from the Ti:Sapphire, with frequencies ω_1, ω_2 and ω_{pr} as explained above in *Figure 21* are passed through a scanner. These pulses are then directed into the microscopic objective which then focuses these beams on to a sample placed on the microscope (picture of the microscope is given in *Figure 24*) slit.

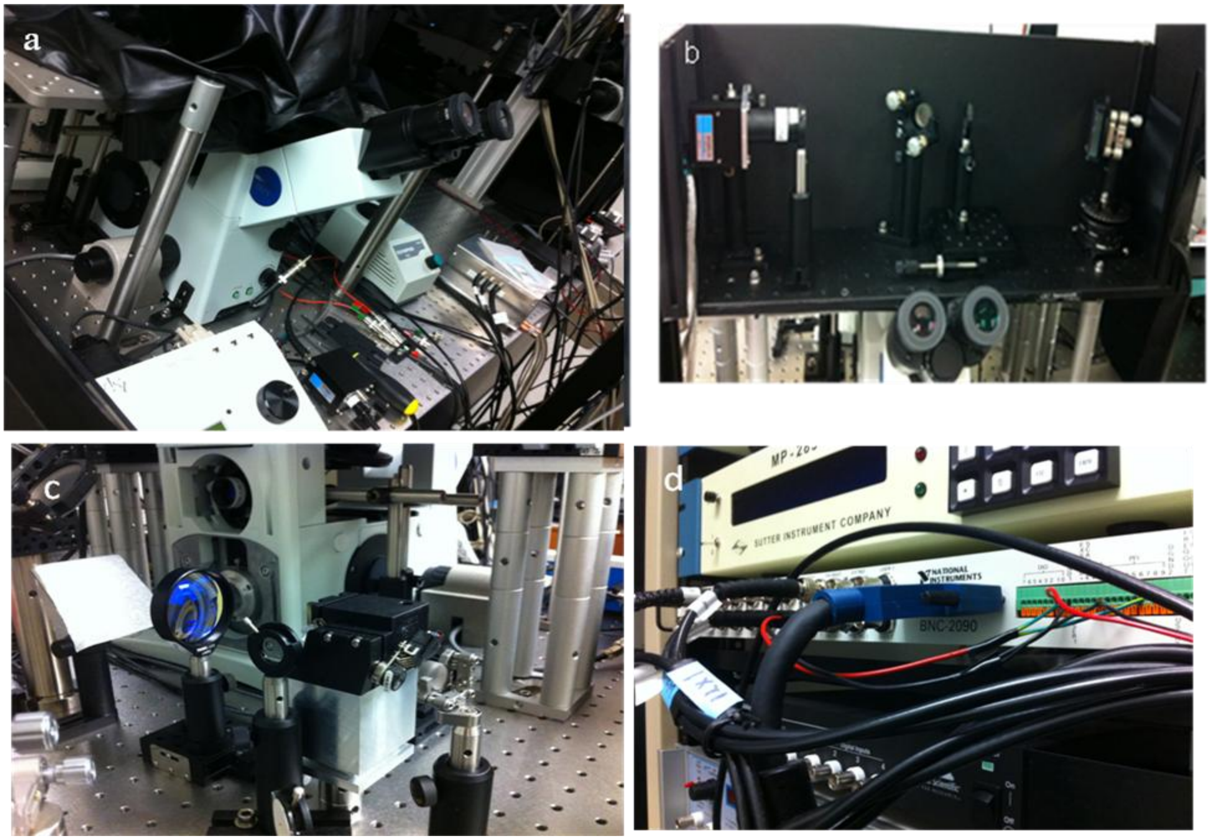

Figure 24: Picture of (a) Microscope, (b) Photo Multiplier Tube (PMT) box with grating for acquiring signal (c)Scanner and (d) NI-BNC 2090 Card

The signal is collected by condenser lens passed through the diffraction grating (shown in right edge of *Figure 24.(b)* and the wavelength of desired frequency is collected by the PMT (shown in left edge of the *Figure 24.(b)*) after passing through the band pass filter(BP). This is shown in detail in the picture and layout shown in *Figure 24*,*Figure 25*)

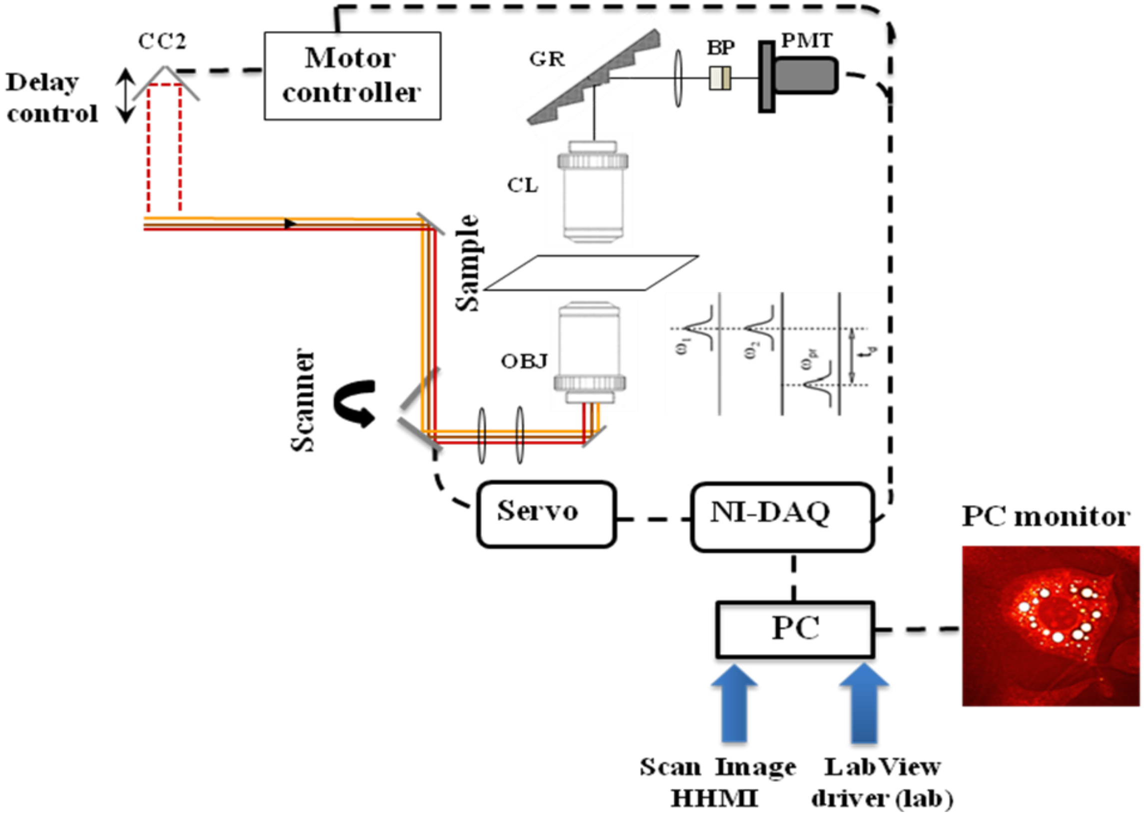

***Figure 25:* Imaging and data acquisition setup was used to probe the coherence in the focal plane of the objective lens (OBJ). BS-beamsplitter mirrors, P1 and P2 – external dispersive prisms used for pulse precompensation, DM-dichroic mirrors, SM-galvo scanner mirrors, CL – condenser lens, GR-diffraction grating.**

Since my thesis mainly concentrates on CARS imaging and spectroscopy, I will explain the setup for the generation of CARS signal in detail. CARS technique derives its detection sensitivity from Raman active molecular vibrations that can be brought in phase within a confocal volume by two short pulses at central frequencies of ω_1 and ω_2 with the difference between the two matching the vibration frequency (Ω_R). A third pulse at ω_{pr} serves as a probe and is scattered into a pulse at anti-Stokes frequency $(\omega_{as} = \omega_{pr} + \Omega_R)$. By delaying the probe pulse one can directly measure subsequent dephasing of the coherent vibrations due to various inter- and intra- molecular interactions. Phase-matching condition is greatly relaxed for small interaction lengths (L). By expressing resonant nonlinear polarization for CARS process in terms of Raman scattering cross-section σ_R [32] one can estimate resonant CARS signal at its

`

maximum (I_{CARS}^{max}). Under a steady state condition the wave equation for anti-Stokes field [2] driven by the nonlinear polarization yields in:

$$I_{CARS}^{max} = \left(\frac{16\pi^2 c^2}{\omega_{as}^3 n^2 h\Gamma} NL\sigma_R \right)^2 I_1 I_2 I_{pr} \qquad (45)$$

Where N is the molecular density, 2Γ is the line width (FWHM) of vibrational resonance, n is refractive index at ω_{as}, $I_{1,2,pr}$ are the focused beam intensities at the corresponding optical frequencies. Considering well characterized 992 cm^{-1} Raman active vibration of benzene (2Γ=2.3 cm^{-1}, σ_R =2.7×10^{-29} cm^2 [33], N=6.8×10^{21} cm^{-3}) as an example one can estimate CARS signal power of ~2 *photons/pulse* that can be produced within focal volume of high NA~1 objective lens. The estimate assumed that 100 *fs* pulses of moderate energy (<1 *nJ*) are used in microscopy arrangement in order to avoid photo damage effects. The generated power translates to a photon flux of about 10^8 *photons/s* for high repetition rate (76 *MHz* in our case) laser system. The output photocurrent of a high gain (>10^6) photomultiplier Tube (PMT) detector is then about 6 orders of magnitude higher than the detector's typical dark current.

3.4. Data acquisition and automation control.

Since the experimental setup consists of combining two OPOs beam in time and space, delaying the third (probe beam), scanning with a galvo, collecting the data with a PMT, we need to synchronize the working mechanisms of the scanner, translational stage, and PMT, with a computer using LabView and MatLab codes. The details of LabView and MatLab codes and screenshots are provided in the appendix section. The translation stage which moves the CC back and forth is controlled by NI-6361 which is automated by labview program installed in the computer. The galvo scanner are controlled by NI-BNC 2090 which are automated by scanimage toolbox of MatLab which is installed in another computer. For acquiring the image we use the MatLab and for acquiring signal vs time delay (spectroscopic information) we use the LabView on the first computer. We believe that with specially designed data acquisition system and software we should be able to probe pixel size structures within a live cell or tissue and reliably obtain CARS transients for specific molecular vibrations.

`

Chapter 4

Results and Conclusions

The results and conclusions are divided into three sections which are; 1) characterization of OPOs for generating tunable femtosecond transform limited pulses, 2) CARS microscopy and micro-spectroscopy of soft condensed matter, and 3) CARS spectroscopy of phonon modes on KTiOPO4 (KTP) crystal pulses.

4.1. Broadly tunable femtosecond optical parametric oscillators based on periodically poled lithium Tantalate crystal.

The first part of this chapter reports the investigations on a broadly tunable femtosecond OPO based on PPSLT crystal. Extensive measurements and characterization of the OPO are focused to study threshold, power, tuning and temporal characteristics of Ti:Sapphire pumped PPSLT OPO. We put a significant effort to find limiting processes and mechanisms that affect output power and that can result from intensity dependent loss in the gain medium. Data shows that the loss results in a significant output power rollover for the OPO at higher pump power. We explore a solution that allowed us to significantly avoid power limitation mechanisms which we believe are primarily due to ultrafast Kerr nonlinearity. The high nonlinear refractive index for PPSLT results in self- and cross-focusing of the resonated signal wavelength beam at high intracavity signal and pump pulse power levels. I present a correlated set of experimental data on OPO output power and pump-power dependent pulsewidth variations. This is obtained for output pulses tunable across the wavelength range of interest (900-1350 *nm*) . I will also present the results of the PPSLT OPO performance at repetition rate harmonics and demonstrate tunable femtosecond pulses at rates of 500 MHz and higher.

Figure 26 shows basic tuning, gain and threshold calculations for the OPO within the wavelength range of interest. In this calculations temperature dependent Sellmeier equations for the pump (n_p), signal (n_s) and idler (n_i) refractive indices are taken from work by Bruner et al.[34].

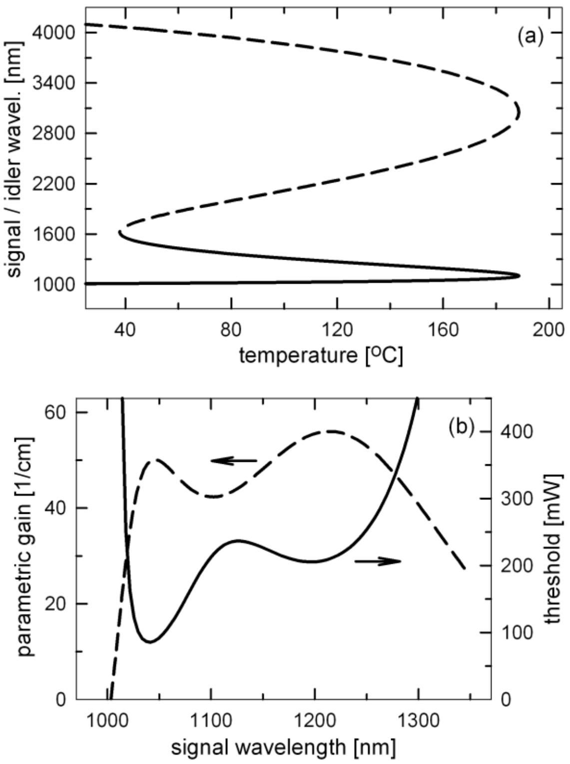

Figure 26: Wavelength tuning curve versus temperature (part (a)), calculated parametric gain and oscillation threshold for PPSLT material based OPO. Sellmeier relations are obtained from work published by Bruner et al[34], quasi-phase matching (QPM) period (Λ) was set to 23.0 μm and the pump wavelength is 810 nm. (a) Wavelength tuning curve versus temperature for signal and idler waves. In (b) left scale corresponds to single pass parametric gain for 1 mm long PPSLT crystal held at 155˚C . Right scale indicates average power threshold for linear resonator with 10% output coupler and additional intracavity loss of 1%.

The single-pass parametric gain shown in part *(b)* of the *Figure 26* is estimated at fixed crystal parameters using the following formula [35]:

$$G(L_c) = \frac{2\omega_s \omega_i d_Q^2 I_p}{n_p n_s n_i \varepsilon_0 c^3} L_c^2 sinc^2\left(\frac{\Delta k L_c}{2}\right) \tag{46}$$

In the equation (46) above, d_Q = 6.75 *pm/V* [36] is the effective nonlinear coefficient of the crystal, L_c is the crystal length and I_p stands for pump power density in the crystal. The data show that a substantial and very broad parametric gain is available in 1*mm* long PPSLT crystal at fairly moderate average power ~1*W* that can be delivered by 76 *MHz* repetition rate mode-locked Ti:Sapphire oscillator. The broad parametric gain ensures broad wavelength tunability that can

`

be performed by changing cavity length. The estimated OPO threshold for these parameters are outlined in *Figure 26*, pump beam spot size is 20 *μm*, pump pulsewidth of 100 *fs*. For a total cavity-roundtrip loss of 10% the oscillation threshold is within 85-250 *mW* range for 250 *nm* bandwidth around 1100 *nm* wavelength. Thus, at least two OPO cavities can be pumped using output of high-power Ti:Sapphire oscillator. With such low threshold and high gain pump depletion in the gain medium which is estimated to be within 60-70% (see *Figure 26*). This should translate into a few hundreds of milliWatts in average output power at signal wavelengths. The following equations are employed to calculate the pump depletion coefficient (η) and available output signal pulse power (P_s) from the OPO cavity with resonating wavelength (λ_s) [37].

$$\eta = 1 - \frac{P_{th}}{P_{in}} - \int_{0}^{ln(P_{in}/P_{th})} cos^2(\Gamma(x)) exp(-x) dx \tag{46a}$$

$$sinc^2[\Gamma(x)] = \frac{P_{th}}{P_{in}} \exp(x) \tag{46b}$$

$$P_s = \eta \frac{T_{OC}}{\alpha + T_{OC}} \frac{\lambda_P}{\lambda_S} P_{in} \tag{47}$$

P_{th} is the pump pulse power at the oscillation threshold, P_{in} is the input pump power at the crystal's facet, $\Gamma\ (x)$ is the stationary gain value at a particular pump power, T_{OC} is the transmission coefficient of the cavity output coupler and α is the intracavity cavity loss due to optics.

4.1.1. Optical Parametric Oscillator Cavity without Dispersion Compensation

Tight focusing condition for the resonator is initially investigated using a 7.5 *cm* focal length lens (L1) with the pump beam passing through two 10 *cm* radius of curvature mirrors (HR1 & HR2). A symmetric bow-tie OPO cavity configuration is realized with physical length of about 987 *mm* for OPO oscillation at about a 152 *MHz* repetition rate (i.e. at second harmonic of Ti:Sapphire repetition rate). The lower oscillation threshold was achieved by matching the resonating signal and pump beam spotsizes [38]. The spotsizes for fixed wavelength (~800 *nm*) pump and the tunable (900-1350 *nm*) signal beam are estimated to be 20 *μm* and 22-25 *μm* respectively. This values are close to ones corresponding to edge areas within the cavity stability range. For the parameters mentioned above and for 1*W* average pump power, power density of about 40 *GW/cm*^{2} is reached within the crystal. This value is an order of magnitude higher than the intensity damage threshold reported for periodically poled lithium niobate (PPLN) crystal for sub-nanosecond pulses [39].

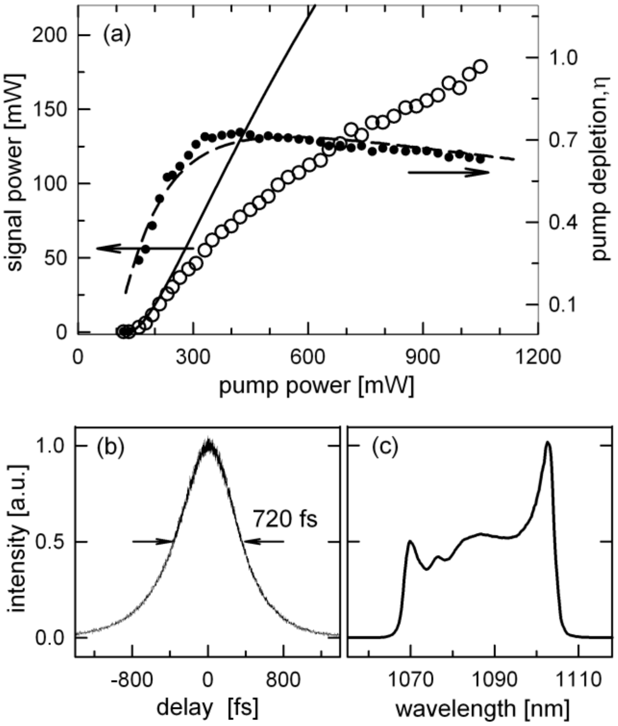

Figure 27: (a) Output power of signal beam (open circles and left scale data) and pump depletion -indicated by solid points- versus pump power from the OPO without dispersion compensating prisms in the cavity. OPO operates at λ_s~1085 nm (Λ = 23 μm, T = 160 °C, λ_p= 810 nm). Solid and dashed lines show calculated results for power and depletion curves respectively. (b) Signal pulse auto-correlation for the OPO cavity pumped with ~ 1.1 W power (i.e. about 10 times above the threshold). (c) The corresponding spectrum of the signal pulse.

Output power for signal beam and pump depletion data are shown in *Figure 27*(a). We managed to attain the threshold of operation (P_{th}) as low as 100 *mW*. This is in good agreement with theoretical value of threshold (see *Figure 27(b)*). Pump depletion curve is also in a good agreement with the model. The experimental depletion data are fit using following equations.

$$\begin{aligned} \eta &= 1-\frac{P_{th}}{P_{in}}-\int_0^{\ln(P_{in}/P_{th}}\cos^2(\Gamma(x))\exp(-x)dx, \\ \sin c^2\left[\Gamma(x)\right] &= \frac{P_{th}}{P_{in}}\exp(x). \end{aligned} \qquad (47)$$

Experimental data for the output power dependency versus pump power (or output power curve) shows a striking difference between the model and experiment. For the calculated power curve using the formula shown below assuming the additional cavity loss (α) is 0.01,

$$P_s = \eta\frac{T_{OC}}{\alpha+T_{OC}}\frac{\lambda_p}{\lambda_s}P_{in.} \qquad (48)$$

In particular , the slope only agrees with the model for pump power levels that are less than $2\times P_{th}$. Likewise, the output power at ~1 *W* pump is about a factor of two less than the expected value. It has to be noted that at 1 *W* of pump power the intracavity signal power is about 1.7 *W*, if one takes into account the transmission of the output coupler used in this case. The combined power density on the crystal from the two color pulses is thus estimated to be at about 60 GW/cm^2 taking into account spot-size diameter and pulse width for the corresponding beams. For incident average pump powers of about 1.3 *W* and higher the crystal damages irreversibly as a result of surface or bulk optical breakdown. *Figure 27(b,c)* shows the signal pulse autocorrelation and spectrum for an average pump power of about 1.1 *W*, about ten times above the threshold condition ($P_{in}\cong 10\times P_{th}$). The signal pulse is more than four times broader than the pump while the spectral width indicates a strongly chirped pulse with a time-bandwidth product of about 4.3. Based on the spectral data we can conclude that significant pulse broadening originates from linear pulse chirp of the signal due to multiple passes through the gain crystal and reflections from the intracavity optics during the buildup time.

Experiments are first conducted with the pulse group delay dispersion (GDD) compensation using a pair of external prisms made of SF10 glass material. By this method the pulse was compressed to nearly the pump pulse duration after a double pass through the pair for a tip to tip separation of about 800 *mm*. The corresponding autocorrelation trace is shown on *Figure 28(a)* in a thin line in comparison with the uncompensated pulse (bold line).

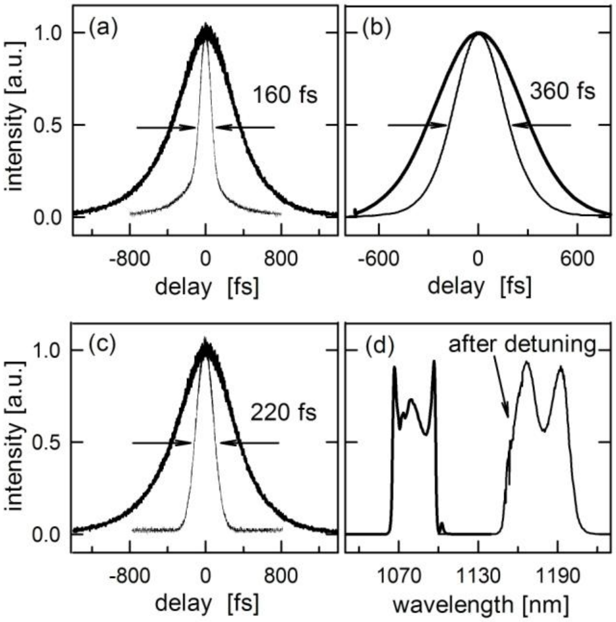

Figure 28: (a) Typical signal pulse auto-correlation function for the case of the externally compensated output signal pulse is shown in thin line compared to the uncompensated signal pulse (bold line). (b) Signal pulse auto-correlation at a pump power of ~250 mW shown in comparison autocorrelation (bold line) corresponding to the case when the OPO was pumped at 1.1W. (c) Signal pulse auto-correlation for the OPO cavity without dispersion compensation when the cavity length was slightly detuned in length (d) Signal pulse spectra for the length matched and detuned cases.

The compressed pulse is still phase-modulated with a time-bandwidth product of $\Delta\nu \times t_p \cong 0.9$ (where $\Delta\nu$ is the pulse bandwidth and t_p the pulsewidth) and a significant amount of nonlinear chirping due to the high level of pump power ($P_{in} \cong 10 \times P_{th}$) [40] as well as self-phase modulation in the nonlinear crystal. This is supported by the result shown on *Figure 28(b)*. The external prism dispersion compensation was not used for this case. In this plot an autocorrelation trace for OPO operation at the high pump power condition (bold line) is compared with a trace for which the pump power is approximately two times above the threshold (thin line). The signal pulse spectrum for the lower pump power case is a factor of two narrower and the pulse broadening due to positive GDD in the nonlinear crystal is less pronounced. Also, at proper cavity length detuning, it is possible to achieve intracavity signal pulse shortening due to pulse formation in the gain medium on the trailing edge of the pump pulse [41, 42] so that its leading edge sharpens. The result is shown in *Figure 28(c)* for 1.1 W of pump power. As expected, the cavity length detuning also leads to a wavelength shift shown in *Figure 28(d)* at the specified rate.

4.1.2. Signal Beam Power Rollover in Optical Parametric Oscillator with Intracavity Dispersion Compensation

Two SF10 prisms separated apart by about 195 *mm* (tip-to-tip), a distance corresponding to cancellation of the positive GDD (about 190 fs^2 at 1100 *nm*) accumulated per roundtrip within the 1 *mm* long crystal. We took into account the intracavity beam spotsize and varying insertion of the beam into the prism material for different wavelengths of operation. *Figure 29(a)* shows the OPO output power curve when the central wavelength is tuned to ~1090 *nm*, close to the wavelength of the *Figure 27* data for which no prisms are used. The OPO was aligned to its lowest threshold with the intracavity prisms inserted to produce the shortest pulse and stable output. The pump depletion is close to the level observed for the uncompensated cavity. The output power curve shows a clear rollover in the vicinity of 1 *W* pump power thus limiting the output power to about 150 *mW*. This value is about 20% lower than the output power produced for the resonator without intracavity dispersion compensation (see again *Figure 27(a)*) and is obviously well below the calculated value based on the model outlined above.

`

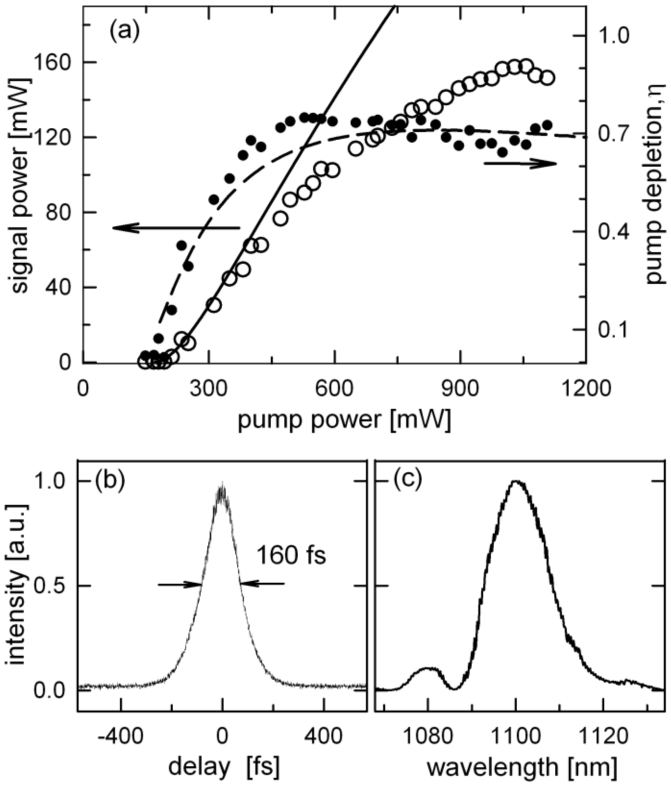

Figure 29: (a) Average power at signal wavelength (open circles) and pump depletion (solid points and right scale data) from the dispersion compensated OPO. The OPO operates at ~ 1100 nm. Solid and dashed lines are the calculated curves for the model used (see text). (b) Typical signal pulse auto-correlation for the OPO. (c) Signal pulse spectrum and pulsewdith correspond to time-bandwidth product of $\Delta\nu \times tp = 0.42$ for hyperbolic secant pulse shape.

As mentioned the prism insertion corresponded to minimization of the net GDD as evidenced from the autocorrelation data shown in *Figure 29(b)* indicating a pulsewidth as short as 103 *fs* (*sech*^{2} shape was assumed). This results in a time-bandwidth product of 0.42 (30% above the value for a transform limited pulse) when taking into account the spectral bandwidth (see *Figure 29(c)*). *Figure 30* shows a similar set of data at signal wavelengths tunable around 1 *μm*. As stated previously this wavelength range is of interest for nonlinear microscopy and it is not easily attainable by Ti:Sapphire laser. Also, previous studies did not demonstrate a detailed characterization of OPO performance within this range. In order to obtain this wavelength range around 1 *μm* we chose a QPM period of 20.6 *μm* and pump wavelength of 746 *nm*. The corresponding wavelength tuning curve versus temperature has a similar shape as that shown in *Figure 26* leading to broadband gain at a set temperature.

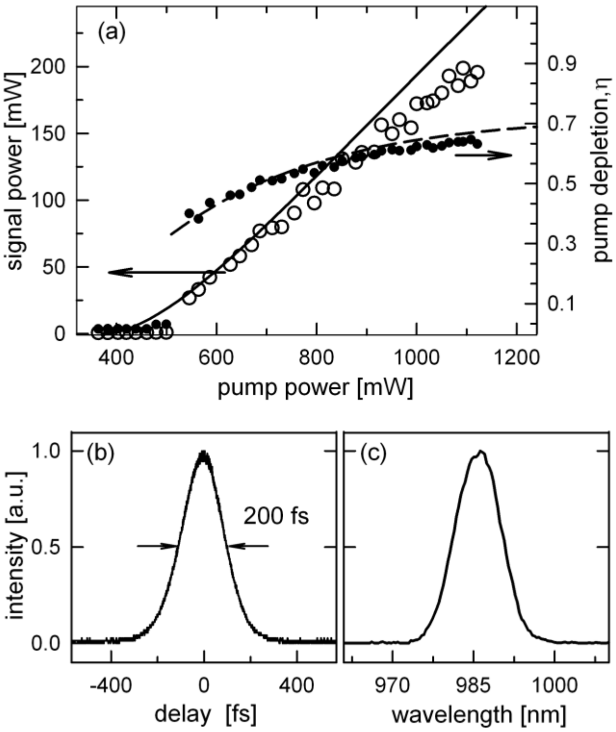

Figure 30: (a) Signal beam average power and pump depletion (solid points, refer to right scale) from the dispersion compensated OPO operating at λ_s = 985 nm. The calculated data are shown in solid and dashed lines correspondingly. (b) signal pulse auto-correlation for the OPO. (c) The corresponding spectrum of the signal pulse.

The OPO output versus pump power at a central wavelength of 985 *nm* is shown in *Figure 30(a)*. The data shown here correspond to the use of a slightly non-collinear pump geometry which, due to less than optimal overlap of pump and signal beams as well as larger signal spotsize in the crystal, led to a higher threshold of operation (about 475 *mW*). This condition coupled with a cavity with a higher positive GDD value (longer pulse) results in higher average power output at 1*W* pump power compared to low threshold operation with GDD near zero (shorter pulse). Also the pump beam depletion is close to 70% and the depletion data can be accurately fit using the above threshold value, The OPOs output power curve shows closer agreement with the model.

Thus, the data presented up to this point can be summarized with the following observations. (i) The OPO shows low threshold levels within a broad wavelength range at fixed temperature and QPM period in good agreement with theoretical estimates for PPSLT crystal. (ii) The gain material was found to sustain peak power density levels as high as 60 *GW/cm*^{2} for

`

femtosecond pulses (~100 *fs*) at near-IR wavelengths before optical breakdown occurs. (iii) One of our main observations is that the detected OPO average power was found to be significantly lower than that predicted by the theoretical model. The signal power dependency versus pump power follows the theoretical model only at pump power levels not exceeding approximately two times threshold. Above this power there is a significant decrease in the corresponding slope followed by the output power rollover. The pump depletion curve may also significantly deviate from the calculated results that rely on the established model [37]. A higher average power can be obtained when the OPO cavity GDD is adjusted to positive values thus resulting in longer pulses (lower peak power) at the output. Nearly zero GDD for the cavity results in lower average power or unstable operation.

4.1.3. High power Optical Parametric Oscillator Operation under 'soft' focusing conditions.

Lastly, to further confirm the concept that nonlinear refraction affects power scaling and conversion efficiency of the PPSLT OPO and in an attempt to optimize the OPO performance we have modified the resonator. In order to reduce peak power densities in the crystal at a fixed average power and thus the power dependent loss we used larger radius of curvature mirrors and a larger focal length lens for the pump beam (L1). This increases the pump and signal spot size diameters by an approximate factor of 1.6 (soft focusing condition). The expectation is that the available peak power before the onset of significant loss will increase by a factor of 2.5. Under these conditions the depletion data can be fit well using equation (2) of the original model. Also, we can now achieve average powers of about 250 mW for shorter pulses (~110 *fs*). The corresponding peak power now reaches approximately 35 *kW*, the expected factor of 2 larger than that obtained using the tight focusing condition with the same pulsewidth. The threshold of operation, however, has increased as a result of the larger spotsize diameters for the beams. Further, if we again use a slightly noncollinear geometry of interaction between pump and signal beams we can achieve average power levels close to 500 mW for longer signal pulses (~165 *fs*) by introducing more positive GDD through prism insertion. The corresponding peak power is close to 40kW. The noncollinear interaction (less than 3 ° in the external angle) along with longer pulses further mitigates the effect of power dependent loss. The high parametric gain delivered by the PPSLT crystal allowed us to configure the OPO to run at higher repetition rates corresponding to harmonics of the pump laser [43].

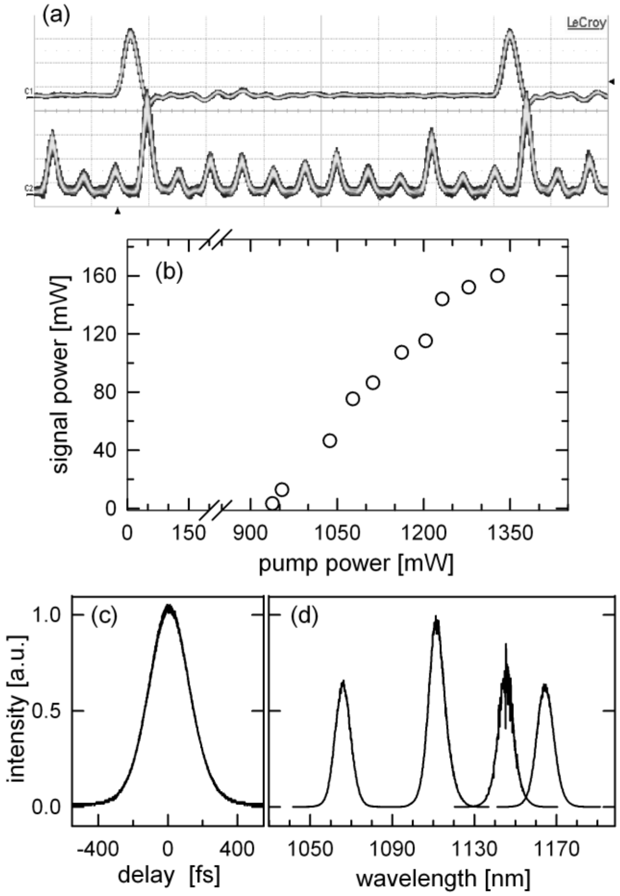

Figure 31: (a) Oscilloscope traces of the mode-locked Ti:sapphire pump laser (upper trace) and fs OPO (lower trace) operating at 12th harmonics (912.5 MHz) of the pump repetition rate. (b) Power curve for the OPO operating at 7th harmonics (532.3 MHz). The OPO crystal parameters and settings are the same as for the data presented on Figure 27.(c) Pulse autocorrelation at the central wavelength (λ_s = 1110 nm) of the tuning range. (d) The high repetition rate (532.3 MHz) OPO spectra across the tuning range. The average power at edges of the tuning range dropped by less than 30% from the power at the central wavelength.

Figure 31 shows oscilloscope traces for the OPO pulse train at pump (upper trace) and signal (lower trace) wavelengths detected by broadband photodetectors. We observed stable operation of the OPO at 912.5 *MHz* for dispersion for an uncompensated cavity, which represents the 12-th harmonic of the fundamental when the cavity length was increased by 1/12 of its original value. The dispersion compensated OPO delivered as high as 160 *mW* (see part *(b)* of the *Figure 31*) in average power at 532.3 *MHz* repetition rate (7-the harmonic) with pulsewidths in the range of 180-230 *fs* without a need for active cavity stabilization. Under this condition the high-repetition rate OPO was tunable within the 1065–1170 *nm* range by micrometer length tuning with the representative spectra shown on part *(d)* of the *Figure 31*.

4.1.5. Conclusion.

Results reporting a detailed investigation on power, tuning and temporal characteristics of a Ti:Sapphire pumped femtosecond OPO based on PPSLT crystal that allows broad (900-1350 *nm*) tuning in the near infrared are presented. It has been confirmed that, given the high parametric gain of PPSLT, low oscillation thresholds can be achieved at about a 100 *mW* average pump power level. The significant finding of this work is that the peak and average power scaling is strongly affected by the onset of intracavity power dependent losses. Specific experiments and results suggest that these losses are due to self- and crossbeam- focusing of the resonating signal beam resulting from the fairly high nonlinear refractive index of lithium tantalate. It is evident from the results that optimization of the OPO performance is possible by utilizing methods leading to the reduction of peak power density in the gain crystal without significantly increasing the oscillation threshold.

4.2. CARS microscopy and micro-spectroscopy of soft condensed matter.

This part of this thesis reports on the realization of three-color time-domain CARS microspectroscopy and imaging with tunable femtosecond pulses delivered by independently tunable high-repetition rate OPOs. Experimental results shows more than five orders of magnitude in time-domain CARS signal detection while the signal was generated from sub-femtoliter probe volumes. The achieved sensitivity provided precise information on complex vibrational spectra of aqueous and viscous media that exhibit weak Raman lines. Approach in live cell imaging and quantitative analysis are also demonstrated. Time-resolved CARS have been previously reported with regard to microscopy applications using *multi-kHz fs* laser system [44], chirped pulses [45] and two-pulse time-resolved CARS [46]. Our approach and implementation demonstrate orders of magnitude higher sensitivity and thus stronger potential for quantitative imaging of live biological media with high spectral and spatial resolutions. The broadly tunable near-infrared OPOs that are specifically designed for this case are optimal from standpoints of reduced photo damage effect and utilization of high numerical aperture objective lenses in order to achieve ultimate spatial resolutions.

4.2.1. Independently tuning optical parametric oscillators.

Tuning range that enables access to characteristic Raman active vibrations of major protein and DNA rich structures are used in this experiment. The OPO and Ti:sapphire beams average power are adjusted to the total power level of 50-60 *mW* in the image plane. In the signal detection part the transmitted signals are dispersed by a diffraction grating (1200 *lines/mm*) and the beam at anti-Stokes wavelength is then detected through a bandpass filter by a high-gain PMT(see *chapter 3*). Since the femtosecond excitation and probe pulse spectra ($\Delta\nu_p$) are broad several Raman lines can be excited and probed. In this case (i.e. $\Delta\nu_p >> T_2^{-1}$) and if a cluster of homogenously broadened lines with identical linewidths falls under the ω_1 and ω_2 pulse spectra the convolution integral derived for the coherent time-domain CARS signal [46] can be approximated for positive delay times ($t_d > 2\text{-}3 \times tp$) by a simple expression:

$$I_{CARS}(t_d) \propto e^{-\frac{2t_d}{T_2}} \left| \sum_j A_j e^{i(\omega_1 - \omega_2 - \Omega_{Rj})t_d} \right|^2 \qquad (49)$$

Where A_j -amplitudes account for differences in Raman cross-sections for the individual lines at particular Raman frequencies (Ω_{Rj}) within the cluster. *Figure 32(b)* shows CARS signal decay obtained in glucose solution at $\Omega_R \sim 900$ cm^{-1} [47]. Our data exhibit dominating single exponential decay thus suggesting that the corresponding homogeneous linewidth ($2\Gamma = 1/\pi c T_2$) for this vibration is about 16 cm^{-1}. Further, we probed a special oil sample to demonstrate resolution of complex Raman spectra within rather weak and not well resolved, in spontaneous Raman scattering, lines near 1300 cm^{-1}.

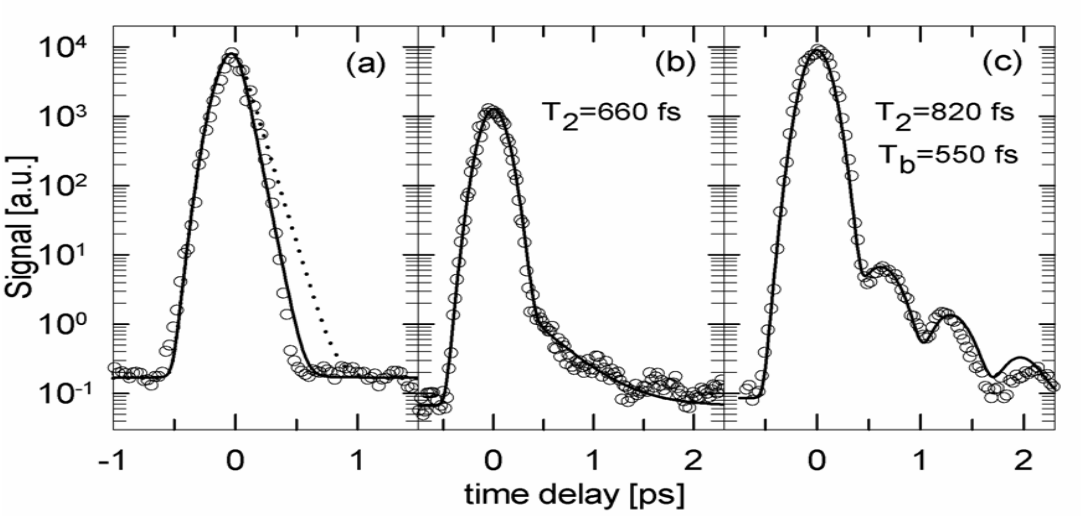

Figure 32: (a) OPO wavelengths are set to 965 nm and 1098 nm respectively (i.e. ω_1-$\omega_2 \cong 1250$ cm^{-1}) to) to generate time-domain CARS signal in coverglass. (b) Time-domain CARS signal obtained from a glucose solution. The measured decay time of 1320 fs corresponds to 16.1 cm^{-1} wide homogeneously broadened line in Raman spectrum. (c) CARS signal for a weak vibrational resonances in oil near $\Omega_R \cong 1280$ cm^{-1} is shown.

The corresponding transient is shown on *Figure 32(c)*. Using a simple model presented by equation (49) we can conclude that the spectrum consists of two lines separated by ~25 cm^{-1} as the quantum beat pattern suggests with individual linewidths of about 13 cm^{-1}. The obtained values are in reasonable agreement with the spontaneous Raman scattering data [48].

4.2.2. Experimental realization of soft condense matter.

In a an attempt to obtain this type of valuable data we imaged a fresh human blood sample with red blood cells adherent to one another. The corresponding image taken at Ω_R=1050 cm^{-1} is presented in *Figure 33(a)*. Further scanning probe delay we have measured time-domain CARS signal while the beams are scanned at the same time across the entire image area. The result presented in *Figure 33(b)* shows close to a resolution-limited response for CARS signal with a best fit achieved for T_2=122 *fs*.

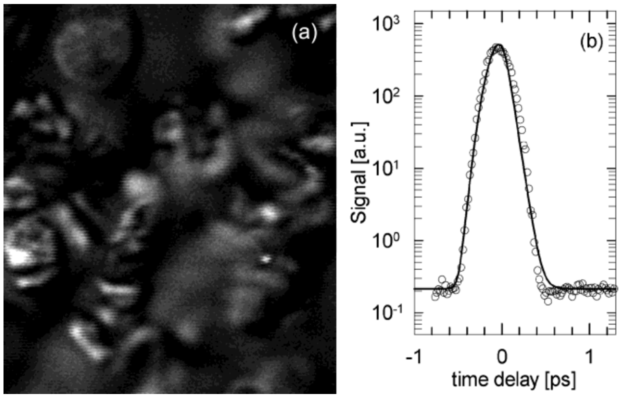

Figure 33: (a) Image (50×70 μm^2) of a human blood sample at ~1180 cm-1 and t_d=200 fs showing densely packed red blood cells with noticeably high resonant CARS signal areas. (b) CARS transient taken on the sample.

The resonant signal was obviously averaged out in this case as the transient was taken while scanning the heterogeneous sample within relatively large area. Implementation of this approach would result in valuable information on specific inter- and intra-molecular interactions within major molecular groups of major cell or tissue constituents. Also we are confident that with certain improvements and optimizations we should be able to detect time-domain CARS signals within 6-7 decades.

4.2.3. Conclusion.

We have implemented three-color CARS microscopy that made possible to track decay of weak and complex Raman modes. The sensitivity ultimately allowed us to obtain information that is specific along three different dimensions (i.e. in spatial, spectral and time domains) that can uniquely and more comprehensively characterize heterogeneous media.

4.3. CARS spectroscopy of phonon modes in a solid state.

4.3.1. Motivation

Decay of the strongest optical phonon mode in $KTiOPO_4$ was directly traced using femtosecond CARS spectroscopy. The Raman active mode at ~700cm^{-1} decays with the nonlinear polarization dephasing time of 495±10 *fs*. The dephasing is solely due to the phonon energy decay with corresponding homogeneous linewidth of 21.4±0.5 cm^{-1}. Low temperature

`

linewidth of 14.7 cm^{-1} is estimated from our data assuming that down-conversion phonon relaxation process is dominant. Our results can help to understand stimulated Raman generation and oscillation of Stokes wave and its harmonics in laser systems where Raman gain is critically dependent on dephasing time.

Efficient solid-state media for Raman amplifiers and frequency converters is of continuous search due to a variety of practical applications (e.g. ultrafast switching, all optical signal processing). After the demonstration of Raman laser action in silicon [49], efforts in this direction have been intensified. Non-centrosymmetric birefringent crystals are an excellent option for the applications since they possess strong Raman active vibrations at higher frequencies (>500 cm^{-1}). Furthermore, birefringent crystals, depending on the cut, can simultaneously generate phase-matched second harmonics or sum frequencies, as reported by Chen [50]. Hence, they can be used for concurrent and efficient generation of multiple wavelengths. An efficient stimulated Raman scattering and frequency conversion have been recently demonstrated in bulk KTP crystal, where depletion values in excess of 50% and a broadband Raman gain of ~60*THz* have been attained [51]. Recently, lasing due to Raman gain has been reported in the near-infrared optical parametric oscillator (OPO) based on periodically poled KTP crystal [52]. The efficiency of the process was shown to be critically dependent on the dephasing rate of coherently driven lattice polarization. Thus, coherent optical phonon dynamics is of practical interest in non-centrosymmetric crystals with high second order nonlinearity.

4.3.2 Time-domain CARS

This section provides experimental results on the high frequency optical phonon decay in bulk KTP crystal at room temperature, measured using time-domain CARS spectroscopy technique with femtosecond time resolution. In the experiments, a strong vibration line at ~700 cm^{-1} (21*THz*) corresponding to one of the fundamental vibrations of TiO_6 octahedra was excited and probed. We provide a direct measurement of the associated nonlinear polarization dephasing and the evidence that the Raman active vibration is homogeneously broadened with the dephasing governed by the optical phonon decay. We conclude that the phonon lifetime for the investigated vibration is 250±5 *fs*. In addition, we can clearly resolve fine structure within the excited phonon band. Spontaneous Raman spectroscopy studies [53-55] reported in the past lack precision and resolution in order to make these conclusions.

Time-domain CARS spectroscopy has been shown as a valuable tool to probe the dynamics of elementary excitations in condensed matter [55, 56]. The method can be viewed as a process of probing the degree of coherence in condensed matter that can be selectively prepared by two ultrashort light pulses. The time-synchronized pulses with optical frequencies ω_1 and ω_2, with the difference matching a vibration frequency (Ω_R), can create a macroscopic nonlinear polarization within a confocal volume by phasing in individual Raman active vibrations. A third pulse at ω_{pr} frequency serves as a probe and is scattered into a pulse at anti-Stokes frequency ($\omega_{as}=\omega_{pr}+\Omega_R$). By delaying the probe pulse, one can directly measure subsequent dephasing of the coherent vibrations due to various interaction processes and infer the corresponding dephasing time constant (T_2) (*Figure 34(a)*). A clarification on the measured dephasing time T_2 is necessary. Loss of phase correlation (or 'pure' dephasing) between individual vibrations probed within the excitation volume can be described by τ_{ph} time. Then, for the measured T_2 time, the relationship $\frac{2}{T_2}=\frac{1}{\tau_{\mathrm{ph}}}+\frac{1}{T_1}$ should hold true [57]. The second ($1/T_1$) term represents energy dissipation rate for the investigated vibrational mode.

The experimental realization of CARS for studying phonon modes in condensed matter was implemented, in the recent past, using different approaches [58, 59]. Here, we demonstrate CARS using synchronized, high-repetition rate (76 MHz), and independently tunable OPO. The laser source consists of two low threshold OPOs designed in our laboratory[31].The experimental arrangement for the three-color time-domain CARS spectroscopy are explained in detail in *chapter 3(experimental setup)* of this thesis

The transmitted signals are dispersed by a diffraction grating, filtered by a bandpass filter, and detected by a high-gain PMT. Using these arrangements, we are able to detect time-domain CARS signal within 5 - 6 orders of magnitude while scanning time delay of the probe pulse with respect to the fixed near-IR excitation. The data for nonresonant signal (*Figure 34(a)*) generated in glass suggest that the nonlinear polarization dephasing times (T_2) as short 100 fs can be measured.

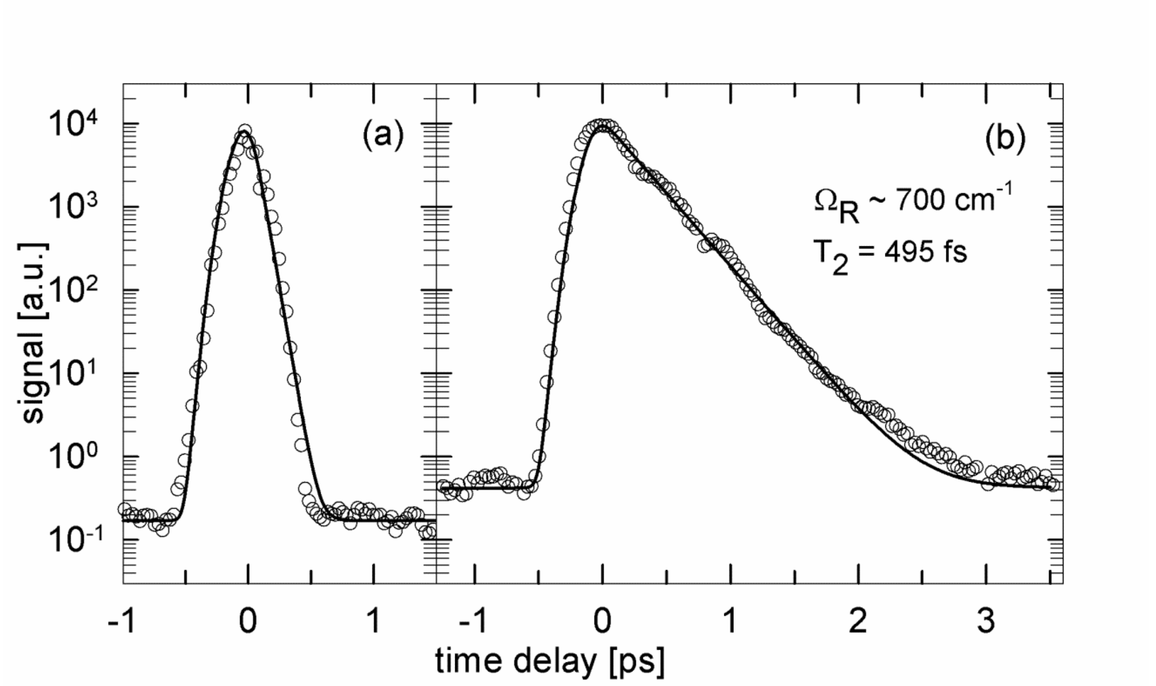

Figure 34: (a) Time-domain CARS signal obtained from glass (open circles) and CARS signal fits assuming dephasing times of 100 fs (solid line)) and 150 fs (dashed line). The experimental noise floor is taken into account for all the data presented in this work.

(b) CARS transient (open circles) for the excited ν_2 (E) (TiO_6 octahedra) vibration in KTP. Solid line shows result of a calculation of the resonant CARS signal using formula (50) and assuming parameters indicated on the plot.

Since the femtosecond excitation and probe pulse spectra ($\Delta\nu_p$) are broad, several Raman vibrations can be excited and probed. In this case (i.e. $\Delta\nu_p >> T_2^{-1}$), if a cluster of homogenously broadened lines with identical linewidths falls under the transform limited pulse spectra, the convolution integral derived for the time-domain CARS signal [70] can be approximated for positive delay times ($t_d > 2t_p$) by the following expression:

$$I^{CARS}(t_d) \propto \sigma^2 e^{\frac{-2t_d}{T_2}} \int_{-\infty}^{\infty} I_{pr}(t'-t_d) \left| \sum_j f_j e^{-i(\omega_1-\omega_2-\Omega_{Rj})t'} \right|^2 dt' \qquad (50)$$

Where σ represents Raman scattering cross-section, I_{pr} is the probe pulse intensity, f_j is the weighting factor for the particular Raman line amplitude within the cluster. The phase-matching factor is neglected in the formula due to small (<1 μm) interaction length. Provided that the time-domain signal is measured over several decades, a precise spectral shape of vibration can be deduced from the Fourier-transformed data [12]. In this case, a much better equivalent spectral resolution, compared to a spontaneous Raman experiment, can be attained.

4.3.3 KTP crystal phonon decay time and phase matching.

The flux-grown KTP crystal used in the experiment was cut at $\phi=40°$ and $\theta=0°$. Thus, both A_1 and A_2 symmetry tensor components are involved[53]. The excitation beams had central wavelengths of 1020 *nm* and 1099 *nm* so that the photon energy difference matched 704 cm^{-1} in Raman frequency, close to the strongest optical phonon line (709 cm^{-1}) in KTP's spontaneous Raman spectra. The mode is assigned to a fundamental vibrations ($\nu_2(E_g)$ asymmetric stretching mode) of TiO_6 octahedra [55]. In the excitation process, momentum conservation must be imposed on the wave vector of the material: $\vec{k}=\vec{k}_1-\vec{k}_2$. Hence, non-zero momentum states can be investigated in forward geometry. The excitation wavevector $k\sim 8\times 10^3 cm^{-1}$ defines corresponding polariton mode with a group velocity of about 0.002*c* estimated using data from Ref.[51]. This makes propagation effect during the time scale of the experiment negligible, thus allowing fairly precise measurements of the corresponding dephasing time.

Figure 34(b) shows time-domain CARS signal, on a semi-logarithmic plot, for the excitation and probe conditions as mentioned above. The resonant contribution is dominant, as can be seen from the shape of the transient, whereas a non-resonant, time resolution limited, peak is absent. The experimental CARS signal shows purely exponential decay as evidenced by almost perfect straight line on the semi-logarithmic plot. The pure exponential decay over several orders of magnitude is an ultimate indication that the Raman line is homogenously broadened [32]. The corresponding Fourier-transform calculations for the data show less than a percent deviation from the Lorentzian lineshape. The solid line on *Figure 34(b)* corresponds to the best fit obtained using formula (50) with time constant T_2 = 495±10 *fs*. This suggests that the corresponding homogeneous linewidth ($\Delta\nu=1/(\pi c\ T_2)$) is 21±0.5 cm^{-1}. We believe that in our case the line broadening is solely due to the loss of vibrational energy. In the KTP crystal, lattice defects and impurities can result in inhomogenous broadening for the probed vibration. As a result, time-domain CARS signal would deviate from the exponential decay and the deviation can be detected with a good precision. This however is not the case for the presented data on

Figure 34(b) and we therefore conclude that defects concentrations are too small to cause any broadening of the vibration. Contributions from residual free carriers can be neglected as well. Indeed, we are probing transverse phonon vibration and there is no associated Plasmon-phonon coupling due to the charged carriers plasma like in the case of longitudinal optical (LO) phonon vibration. Therefore, there is no effect of 'pure' depahsing and $1/\tau_{ph} \rightarrow 0$. The only remaining dephasing mechanism for the nonlinear polarization is the excited phonon energy decay which leads to $T_1=T_2/2$ relationship. Instead, the phonon energy decay is due to anharmonic interactions with other phonon modes [60]. The relevant interaction should satisfy energy and momentum conservation rules for the phonons that are involved in the process. The lowest order (i.e. three-phonon interaction) down-conversion decay process corresponds to the investigated phonon splitting into two phonons of lower energies. The up-conversion process leads the phonon to be scattered by a thermal phonon into a phonon of higher energy. The relative weight of the different processes strongly depends on the symmetry and density of states at zero-wavevector of the associated two-phonon bands. This information on KTP has not been reported in the past. For both up- and down-conversion processes, the associated relaxation rate is related to the occupation number of the final phonons at fixed temperature and thus to their energies [61]. Based on the spontaneous Raman data [53-55], there are multiple combinations for down-conversion process that would satisfy energy conservation rule with many of them involving final phonons having about the same energy (~350 cm^{-1}). Assuming that the down-conversion is indeed a dominant energy relaxation process, we can make an estimate of the anharmonic coupling constant (γ), and thus estimate low temperature linewidth, using the following equation for the phonon rate decay [61]:

$$\Gamma(T) = \gamma\left(1 + \frac{2}{e^{\frac{h\Omega_R}{2kT}} - 1}\right) \tag{51}$$

,where last term represents phonon occupation number with half-energy. Using $\Gamma=1/T_1$, $T_1=T_2/2$ relationships and the measured $T_2 = 0.495$ *ps* time for the phonon at room temperature (T=300 *K*), we arrive to an estimate of $\gamma=2.79\ ps^{-1}$. This yields in linewidth ($\Delta\nu=\gamma/2\pi c$) of 14.7 cm^{-1} as temperature approaches to zero.

`

4.3.3. Experimental realization of phonon decay time in KTP.

Figure 35 shows CARS transient at the condition when the wavelength of OPO$_1$ was slightly tuned to the blue side. The observed quantum beats pattern suggests that two Raman active phonon lines are excited. The lines are spaced 41 *cm^{-1}* apart with the amplitude ratio of about 3:1. The line spacing is just about 10% larger than the value obtained from spontaneous Raman experiments [55].

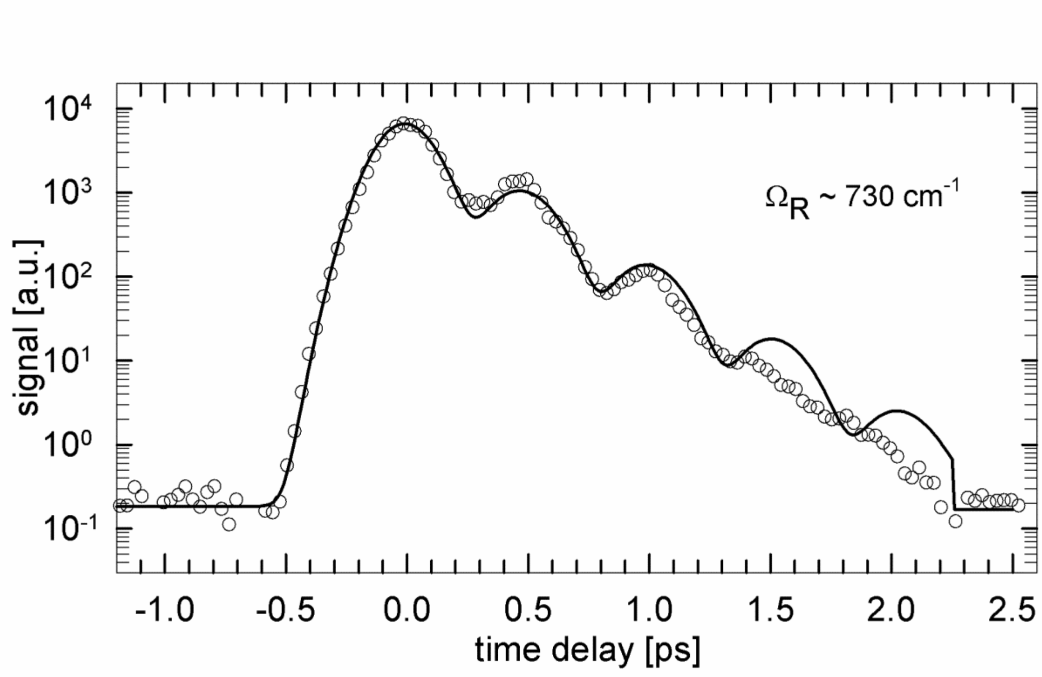

Figure 35: CARS transient (open circles) for the excited $\nu_2(E)$ (TiO$_6$ octahedra) band in KTP at a detuned OPO wavelength favoring excitation of the second peak within the band. Solid line shows result of a calculation for the resonant CARS signal using formula (50) and assuming parameters for T_2=500 fs and frequency difference of 40.7 cm^{-1} between the peaks

4.3.4. Conclusion

High-frequency phonon decay in KTP material was observed. The observed phonon lifetime of 250 *fs* is precisely measured for the strongest phonon band corresponding to the main asymmetric stretching vibration of TiO$_6$ octahedra using time-domain CARS spectroscopy. Assuming that down-conversion process dominates the excited phonon decay, we estimated low temperature phonon line width to be 14.7 *cm^{-1}*.

`

4.4 Summarized Conclusions

We have designed an extremely sensitive CARS setup. The sensitivity and the equivalent resolution entirely rely on independently tunable ‘Optical Parametric Oscillators’ in the near IR region. This Setup performs different type of imaging and spectroscopy; we have shown that we can perform multi modal imaging of live cells and tissue where signals resulting from various nonlinear optical interactions provide complimentary information about the biological media. We have also shown that time domain CARS is capable for measuring critical parameters as concerned to complex Raman vibrations in solid state and soft condense matter. This type of apparatus is unique and doesn’t have any analogues.

`

Bibliography:

1. Boyd, R.W., *Nonlinear optics*. 2003: Academic Pr.
2. Shen, Y.R., *The principles of nonlinear optics*. New York, Wiley-Interscience, 1984, 575 p. Vol. 1. 1984.
3. Roh, W.B., *Coherent anti-Stokes Raman scattering of molecular gases*, 1977, DTIC Document.
4. Mukamel, S., *Principles of nonlinear optical spectroscopy (Oxford series on optical & imaging science 6).* 1999.
5. Morris, M.D. and P. Matousek, *Emerging Raman Applications and Techniques in Biomedical and Pharmaceutical Fields*. 2010: Springer Verlag.
6. Yariv, A., *Introduction to optical electronics.* 1976.
7. Miles, R. and S. Harris, *Optical third-harmonic generation in alkali metal vapors.* Quantum Electronics, IEEE Journal of, 1973. **9**(4): p. 470-484.
8. Wilson, E.B., J.C. Decius, and P.C. Cross, *Molecular vibrations: the theory of infrared and Raman vibrational spectra*. 1955: Dover Pubns.
9. Ganikhanov, F., et al., *High-sensitivity vibrational imaging with frequency modulation coherent anti-Stokes Raman scattering (FM CARS) microscopy.* Optics letters, 2006. **31**(12): p. 1872-1874.
10. Giordmaine, J.A. and W. Kaiser, *Light scattering by coherently driven lattice vibrations.* Physical Review, 1966. **144**(2): p. 676.
11. Allen, L. and J.H. Eberly, *Optical resonance and two-level atoms*. 1987: Dover Publications.
12. D'yakov, Y.E., *Dephasing in steady-state and time-varying spectroscopy.* JETP Lett, 1983. **37**(1).
13. Miller, L., G. Smith, and G. Carr, *Synchrotron-based biological microspectroscopy: from the mid-infrared through the far-infrared regimes.* Journal of Biological Physics, 2003. **29**(2): p. 219-230.
14. Zumbusch, A., G.R. Holtom, and X.S. Xie, *Three-dimensional vibrational imaging by coherent anti-Stokes Raman scattering.* Physical review letters, 1999. **82**(20): p. 4142.
15. Maker, P. and R. Terhune, *Study of optical effects due to an induced polarization third order in the electric field strength.* Physical Review, 1965. **137**(3A): p. A801.
16. Begley, R., A. Harvey, and R.L. Byer, *Coherent anti-Stokes Raman spectroscopy.* Applied Physics Letters, 1974. **25**(7): p. 387-390.
17. Bloembergen, N., *Nonlinear optics*. 1996: World Scientific Pub Co Inc.
18. Evans, C.L. and X.S. Xie, *Coherent anti-Stokes Raman scattering microscopy: chemical imaging for biology and medicine.* Annu. Rev. Anal. Chem., 2008. **1**: p. 883-909.
19. Duncan, M.D., J. Reintjes, and T. Manuccia, *Scanning coherent anti-Stokes Raman microscope.* Optics letters, 1982. **7**(8): p. 350-352.
20. Cheng, J., et al., *An epi-detected coherent anti-Stokes Raman scattering (E-CARS) microscope with high spectral resolution and high sensitivity.* The Journal of Physical Chemistry B, 2001. **105**(7): p. 1277-1280.

21. Hashimoto, M., T. Araki, and S. Kawata, *Molecular vibration imaging in the fingerprint region by use of coherent anti-Stokes Raman scattering microscopy with a collinear configuration.* Optics letters, 2000. **25**(24): p. 1768-1770.
22. Volkmer, A., J.X. Cheng, and X.S. Xie, *Vibrational imaging with high sensitivity via epidetected coherent anti-Stokes Raman scattering microscopy.* Physical review letters, 2001. **87**(2): p. 19.
23. Evans, C.L., et al., *Chemically-selective imaging of brain structures with CARS microscopy.* Optics Express, 2007. **15**(19): p. 12076-12087.
24. Legare, F., F. Ganikhanov, and X.S. Xie. *Towards an integrated coherent anti-Stokes Raman scattering (CARS) microscopy system*. 2005.
25. Potma, E.O., et al., *High-sensitivity coherent anti-Stokes Raman scattering microscopy with two tightly synchronized picosecond lasers.* Optics letters, 2002. **27**(13): p. 1168-1170.
26. Kee, T.W. and M.T. Cicerone, *Simple approach to one-laser, broadband coherent anti-Stokes Raman scattering microscopy.* Optics letters, 2004. **29**(23): p. 2701-2703.
27. Andresen, E.R., et al., *Tunable light source for coherent anti-Stokes Raman scattering microspectroscopy based on the soliton self-frequency shift.* Optics letters, 2006. **31**(9): p. 1328-1330.
28. Andresen, E.R., et al., *Fiber laser-based light source for coherent anti-Stokes Raman scattering microspectroscopy.* Optics Express, 2007. **15**(8): p. 4848-4856.
29. Yakovlev, V. and G.I. Petrov, *Enhancing red-shifted white-light continuum generation in optical fibers for applications in nonlinear Raman microscopy.* Optics Express, 2005. **13**(4): p. 1299-1306.
30. Ganikhanov, F., et al., *Broadly tunable dual-wavelength light source for coherent anti-Stokes Raman scattering microscopy.* Optics letters, 2006. **31**(9): p. 1292-1294.
31. Rowley, J.D., S. Yang, and F. Ganikhanov, *Power and tuning characteristics of a broadly tunable femtosecond optical parametric oscillator based on periodically poled stoichiometric lithium tantalate.* JOSA B, 2011. **28**(5): p. 1026-1036.
32. Laubereau, A. and W. Kaiser, *Vibrational dynamics of liquids and solids investigated by picosecond light pulses.* Reviews of Modern Physics, 1978. **50**(3): p. 607.
33. Abe, N., M. Wakayama, and M. Ito, *Absolute Raman intensities of liquids.* Journal of Raman Spectroscopy, 1977. **6**(1): p. 38-41.
34. Bruner, A., et al., *Temperature-dependent Sellmeier equation for the refractive index of stoichiometric lithium tantalate.* Optics letters, 2003. **28**(3): p. 194-196.
35. Myers, L.E., et al., *Quasi-phase-matched optical parametric oscillators in bulk periodically poled LiNbO3.* JOSA B, 1995. **12**(11): p. 2102-2116.
36. Lobino, M., et al., *Optical-damage-free guided second-harmonic generation in 1% MgO-doped stoichiometric lithium tantalate.* Optics letters, 2006. **31**(1): p. 83-85.
37. Tukker, T.W., C. Otto, and J. Greve, *Design, optimization, and characterization of a narrow-bandwidth optical parametric oscillator.* JOSA B, 1999. **16**(1): p. 90-95.
38. Boyd, G. and D. Kleinman, *Parametric interaction of focused Gaussian light beams.* Journal of Applied Physics, 1968. **39**: p. 3597.
39. Galvanauskas, A., et al., *High-energy femtosecond pulse amlification in a quasi-phase-matched parametric amplifier.* Optics letters, 1998. **23**(3): p. 210-212.
40. Cheung, E. and J. Liu, *Theory of a synchronously pumped optical parametric oscillator in steady-state operation.* J. Opt. Soc. Am. B, 1990. **7**(8): p. 1385.

`

41. Akhmanov, S., et al., *Nonstationary nonlinear optical effects and ultrashort light pulse formation.* Quantum Electronics, IEEE Journal of, 1968. **4**(10): p. 598-605.
42. Khaydarov, J.D.V., J.H. Andrews, and K.D. Singer, *Pulse compression in a synchronously pumped optical parametric oscillator from group-velocity mismatch.* Optics letters, 1994. **19**(11): p. 831-833.
43. Esteban-Martin, A., et al., *High-harmonic-repetition-rate, 1 GHz femtosecond optical parametric oscillator pumped by a 76 MHz Ti: sapphire laser.* Optics letters, 2009. **34**(4): p. 428-430.
44. Volkmer, A., L.D. Book, and X.S. Xie, *Time-resolved coherent anti-Stokes Raman scattering microscopy: Imaging based on Raman free induction decay.* Applied Physics Letters, 2002. **80**(9): p. 1505-1507.
45. Oron, D., et al., *Narrow-band coherent anti-Stokes Raman signals from broad-band pulses.* Physical review letters, 2002. **88**(6): p. 63004.
46. Lee, Y.J. and M.T. Cicerone, *Vibrational dephasing time imaging by time-resolved broadband coherent anti-Stokes Raman scattering microscopy.* Applied Physics Letters, 2008. **92**(4): p. 041108-041108-3.
47. Enejder, A.M.K., et al., *Raman spectroscopy for noninvasive glucose measurements.* Journal of Biomedical Optics, 2005. **10**: p. 031114.
48. El-Abassy, R., P. Donfack, and A. Materny, *Visible Raman spectroscopy for the discrimination of olive oils from different vegetable oils and the detection of adulteration.* Journal of Raman Spectroscopy, 2009. **40**(9): p. 1284-1289.
49. Rong, H., et al., *A continuous-wave Raman silicon laser.* Nature, 2005. **433**(7027): p. 725-728.
50. Chen, Y., *Stimulated Raman scattering in a potassium titanyl phosphate crystal: simultaneous self-sum frequency mixing and self-frequency doubling.* Optics letters, 2005. **30**(4): p. 400-402.
51. Pasiskevicius, V., C. Canalias, and F. Laurell, *Highly efficient stimulated Raman scattering of picosecond pulses in KTiOPO4.* Applied Physics Letters, 2006. **88**(4): p. 041110-041110-3.
52. Pasiskevicius, V., et al., *Enhanced stimulated Raman scattering in optical parametric oscillators from periodically poled KTiOPO.* Applied Physics Letters, 2003. **82**: p. 325.
53. Kugel, G., et al., *The vibrational spectrum of a KTiOPO4 single crystal studied by Raman and infrared reflectivity spectroscopy.* Journal of Physics C: Solid State Physics, 1988. **21**: p. 5565.
54. FURUSAWA, S.I., et al., *Raman scattering study of KTiOPO 4(KTP) single crystal.* Physical Society of Japan, Journal, 1991. **60**: p. 2470-2474.
55. Vivekanandan, K., et al., *Raman and FT-IR spectroscopic characterisation of flux grown KTiOPO4 and KRbTiOPO4 non-linear optical crystals.* Materials chemistry and physics, 1997. **49**(3): p. 204-210.
56. Von der Linde, D., J. Kuhl, and H. Klingenberg, *Raman scattering from nonequilibrium LO phonons with picosecond resolution.* Physical review letters, 1980. **44**(23): p. 1505-1508.
57. Fischer, S. and A. Laubereau, *Dephasing processes of molecular vibrations in liquids.* Chemical Physics Letters, 1975. **35**(1): p. 6-12.

58. Materny, A., et al., *Wave packet dynamics in different electronic states investigated by femtosecond time-resolved four-wave-mixing spectroscopy.* Applied Physics B: Lasers and Optics, 2000. **71**(3): p. 299-317.
59. Lee, Y.J., et al., *Phonon dephasing and population decay dynamics of the G-band of semiconducting single-wall carbon nanotubes.* Physical Review B, 2010. **82**(16): p. 165432.
60. Califano, S., V. Schettino, and N. Neto, *Lattice dynamics of molecular crystals*. 1981: Springer-Verlag Berlin.
61. Cowley, R., *Anharmonic crystals.* Reports on Progress in Physics, 1968. **31**: p. 123.

Appendix

Matlab codes:

```
1)
%Calculation of Coherent amplitude
global f Q
F=sqrt(I1.*I2).*exp(t/T2);
step1=step;
t1=-10*tp1:step1:(max(td)+10*tp1);
for j=1:length(t1)
    [A,I]=min(abs(t-t1(j)));
    F1=F(1:I);
    fex(j)=trapz(F1);
end
Q=f*exp(-t1/T2).*fex;
```

```
2)
%CARS fit for FFT
clear variables
global f Q

%load data to be fitted
fold='/Users/mdobbala/Desktop/data_for_PRL/';
filename0='KTP_700cm-1_decay_m.dat';
dlmread(strcat(fold,filename0),'\t');
delta=200e-15;                                       %shift exp data in time
```

```
`


td=ans(:,1)*1e-15+delta;
texp=td;
cars_s=ans(:,2);
norm=max(ans(:,2));                                 %signal norm. factor
cars_n=cars_s/norm-0.000015;                        %normalized CARS signal
semilogy(td,cars_n,'ko')
xmin=min(td)-250e-15;xmax=max(td)+250e-15;
ymin=0.7*min(cars_n);ymax=1.3*max(cars_n);
axis([xmin xmax ymin ymax])

%excitation pulses
I10=1;tp1=150e-15;                                  %pulsewidth OPO1
I20=1;tp2=150e-15;                                  %pulsewidth OPO2
step=1e-15;
t=-15*tp1:step:(max(td)+15*tp1);
I1=I10*exp(-4*log(2)*t.^2/tp1^2);
I2=I20*exp(-4*log(2)*t.^2/tp2^2);

%Raman line parameters/oscillator strength
R=0.07;
f1=1;
f2=R*f1;

%calculate coherent amplitude's time-domain
%envelope function Q(t) for homogeniously broadened line;

T2=540e-15;
f=f1;
run calc_coherent_A
Q1=Q;                                               %contrib. of the first
Raman line

f=f2;
run calc_coherent_A
Q2=Q;                                               %contrib. of the second
Raman line

f=0;
T2=10e-15;
run calc_coherent_A
Q3=Q;                                               %contrib. of the second
Raman line

w1=2*pi*21.0e12;z1=complex(0,w1);
w2=2*pi*22.7e12;z2=complex(0,w2);
Qtot1=Q1.*exp(z1*t1)+Q2.*exp(z2*t1)+...
    Q3.*exp(z1*t1);                                 %total coherent ampl.

floor=0.5*ones(1,length(t1));
Qtot=(abs(Qtot1)).^2+floor;

%probe pulse I3
I30=1;
tp3=110e-15;
td=-5*tp1:step:(max(td)+5*tp1);
```

`

```
%correlation integral with I3
for j1=1:length(td)
    I3=I30*exp(-4*log(2)*(t1-td(j1)).^2/tp3^2);
    Fd=Qtot.*I3;
    TDCARS(j1)=trapz(Fd);
end
TDCARS_n=TDCARS/max(TDCARS);                             %normalized CARS signal
hold on
semilogy(td,TDCARS_n)
fit_data=[td' TDCARS_n'];
fold1='/Users/mdobbala/Desktop/data_for_PRL/data_for_figures/';
filename1='PRL_Fig2a_CARS_700_cm-1_KTP_theor_fit.dat';
dlmwrite(strcat(fold1,filename1),fit_data,'\t')
exp_data=[texp cars_n];
filename2='PRL_Fig2a_CARS_700_cm-1_KTP_expr_data.dat';
dlmwrite(strcat(fold1,filename2),exp_data,'\t')
```

3)

```
% Calcualtion of mismatch PPLN
function f=mismatch(Tpm)
global l1 l2 l3 L Lq
l=l1;T=Tpm;
run sellmeier_SLT
ns=n;
l=l2;
run sellmeier_SLT
ni=n;
l=l3;
run sellmeier_SLT
np=n;
dkL=sum(2*pi*1000*(L.*(np/l3-ns/l1-ni/l2-1./Lq)));
f=abs(dkL);
```

4)

```
%PPLN tuning curve
clear variables
%addpath('C:\Documents and Settings\mdobbala\My
Documents\FG_previous_work\MATLAB6p5\work_m\x-tals_tuning_curves')
%addpath('C:\Program Files\MATLAB\R2007a\work\mdobbala\PPLN_OPO_tuning')
global l1 l2 l3 L Lq
Np=100;
%number of points
% L=[1.125 1.125 1.125 1.125 1.125 1.125 1.125 1.125] ;
%crystal length in [mm]
L=15;
```

`

```
lp=746.8;                                                    %pump
wavelength in [nm]
    %Lq=[17.6 18.2 18.8 19.4 20.0 20.6 21.2 21.8 22.4 23.0 23.6 24.2 24.8];
%quasiPM-period in [microns]
    %Lq=[23 23.15 23.3 23.45 23.6 23.75 23.9 24.05];
    Lq=20.6;
    li_max=4000;
%cut-off (90 percent .%transmission) in the IR transmission
    ls_min=lp*li_max/(li_max-lp);
    dls=(2*lp-ls_min)/(Np-1);
    ls=ls_min:dls:2*lp;
%signal wl in [nm]
    li=lp*ls./(ls-lp);
%idler wl in [nm]
    T0=20;
    for i=1:length(ls)
        l1=ls(i)/1000;l2=li(i)/1000;l3=lp/1000;
        options=optimset('TolX',1e-2,'TolFun',1e-3,'maxIter',100);
        [Tpm,fval,exitflag]=fminsearch(@mismatchppln,T0,options);
%optimize T to PM
        if exitflag==0
            pm_T(i)=[];
            ls(i)=[];li(i)=[];
        else
            pm_T(i)=Tpm;
        end
    end
    %run filter_tuning_data
    plot(pm_T,ls,pm_T,li,'k-')
    %xmin=20;
    %xmax=220;
    %ymin=0.95*min(ls);
    %ymax=1.05*max(li);
    xmin=30;
    xmax=180;
    ymin=800;
    ymax=li_max;
    axis([xmin xmax ymin ymax])
    summary=[pm_T' ls' li'];

%filename=strcat('pump_',num2str(lp),'nm_period_',num2str(Lq),'micron','.dat'
);
    %filename2save=strcat('C:\Program
Files\MATLAB\R2007a\work\mdobbala\PPLN_OPO_tuning\data_out\',filename);
    %dlmwrite(filename2save,summary,'\t')
    xlabel('temperature [C]')
    ylabel('\lambda_s,\lambda_i [nm]')
    grid on
    %title(strcat('PPLN tuning:','\Lambda=',num2str(Lq),'\mum-
>',num2str(lp),'nm'))
    %text(pm_T(1),li(1)+50,strcat(num2str(lp),'nm'))
```

`

```
5)
%sellmier_SLT
A=4.502483;
B=0.007294;
C=0.185087;
D=-0.02357;
E=0.073423;
F=0.199595;
G=0.001;
H=7.99724;
b=(3.483933*10^-8)*(T+273.15)^2;
c=(1.607839*10^-8)*(T+273.15)^2;
n=sqrt(A+((B+b)/(l^2-(C+c)^2))+(E/(l^2-F^2))+(G/(l^2-H^2))+(D*l^2));
```

```
6)
% Theoritical tuning curve
global l1 l2 l3 L Lq
Np=100;
%number of points
L=1.0;
lp=790.66;
%pump wavelength in [nm]
    Lq=22.4;
    li_max=3500;
%cut-off (90 percent .%transmission) in the IR transmission
    ls_min=lp*li_max/(li_max-lp);
    dls=(2*lp-ls_min)/(Np-1);
    ls=ls_min:dls:2*lp;
%signal wl in [nm]
    li=lp*ls./(ls-lp);
%idler wl in [nm]
    T0=20;
    for i=1:length(ls)
        l1=ls(i)/1000;l2=li(i)/1000;l3=lp/1000;
        options=optimset('TolX',1e-2,'TolFun',1e-3,'maxIter',100);
        [Tpm,fval,exitflag]=fminsearch(@mismatchppln,T0,options);
%optimize T to PM
        if exitflag==0
            pm_T(i)=[];
            ls(i)=[];li(i)=[];
        else
            pm_T(i)=Tpm;
        end
    end
    plot(pm_T,ls,'k-',pm_T,li,'k-')
    summary=[pm_T' ls' li'];
```

LabView codes(Front panel and Block diagrams)

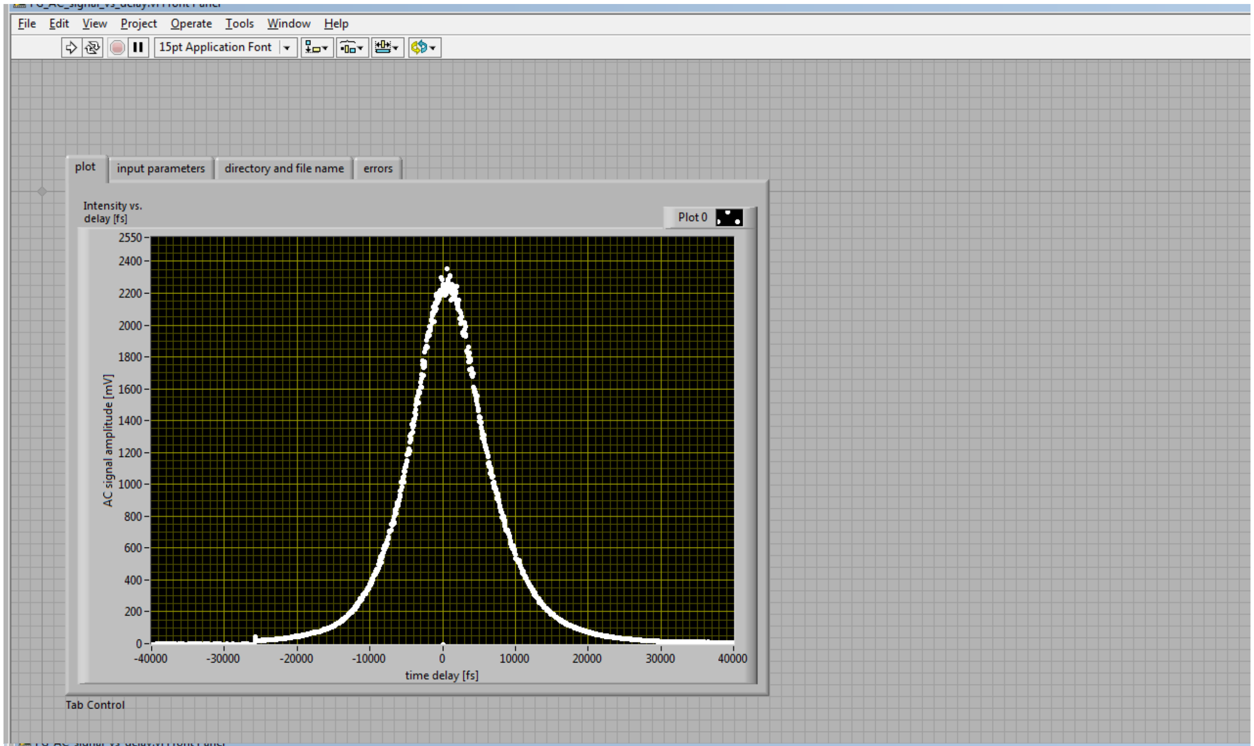

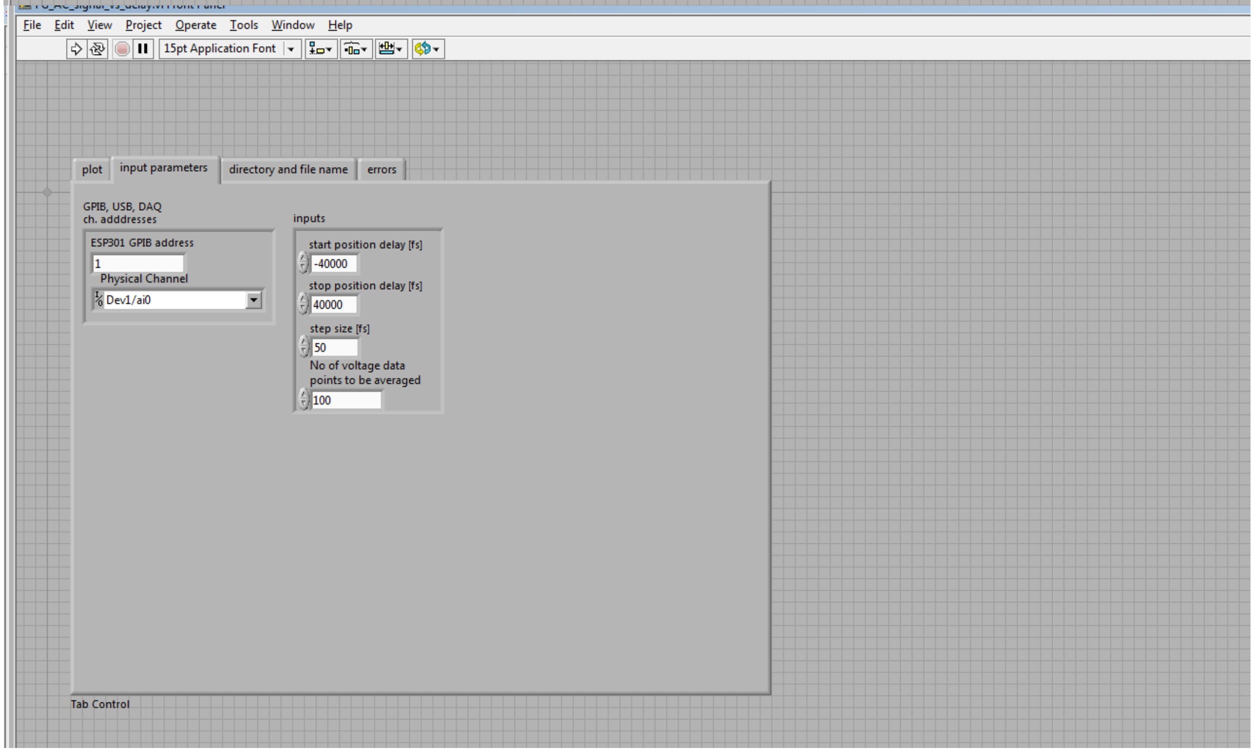

ESP301 GPIB address: 1

Physical Channel: Dev1/ai0

start position delay [fs]: -40000

stop position delay [fs]: 40000

step size [fs]: 50

No of voltage data points to be averaged: 100

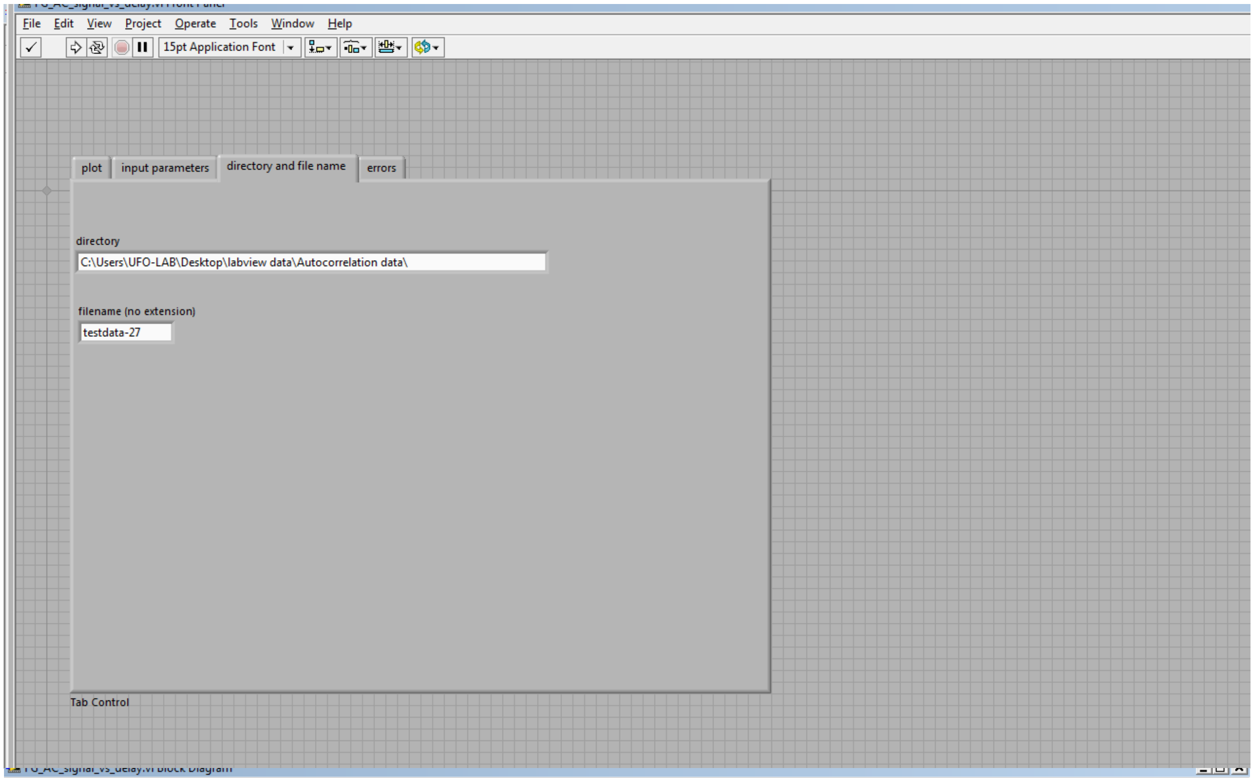

directory
C:\Users\UFO-LAB\Desktop\labview data\Autocorrelation data\

filename (no extension)
testdata-27

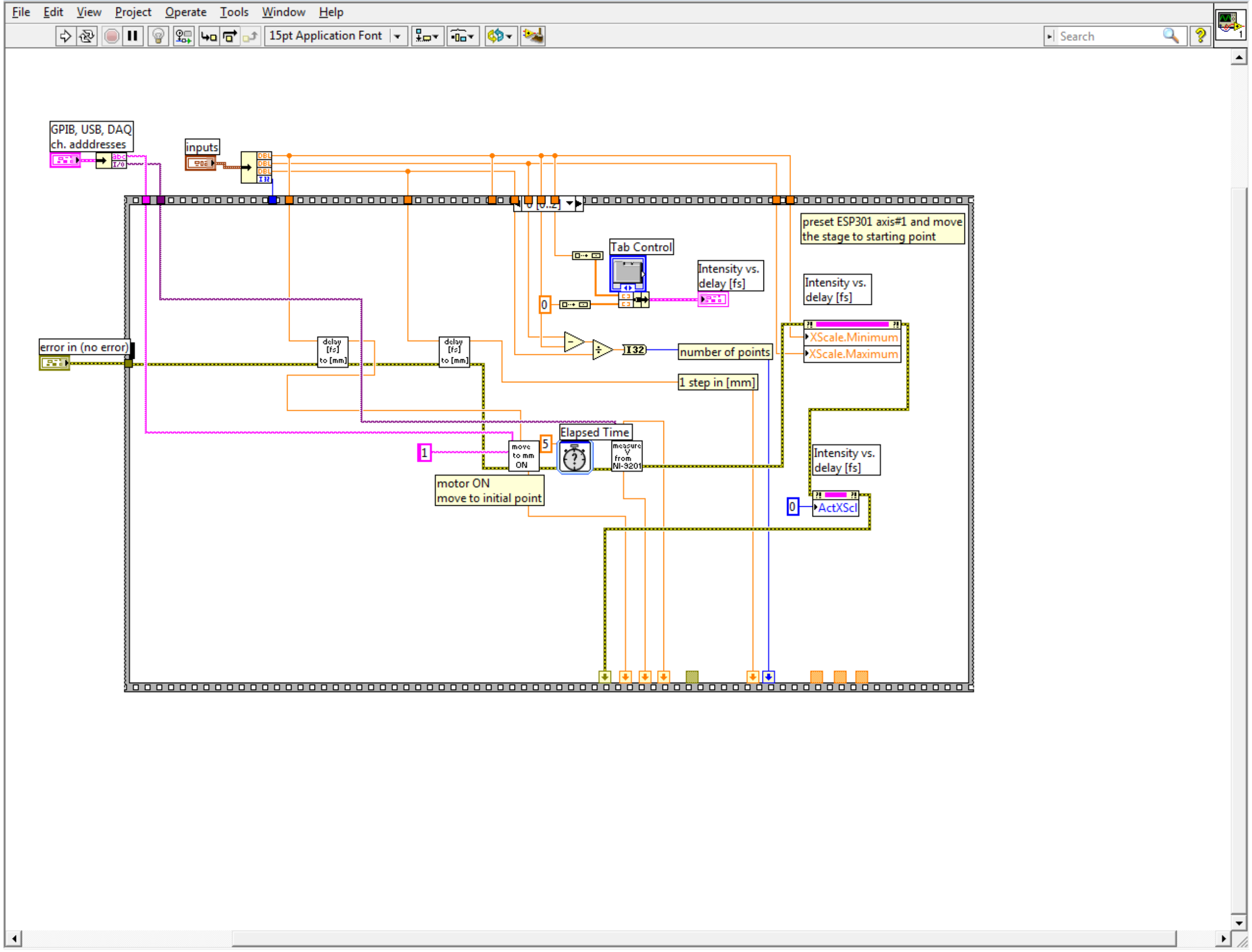

`

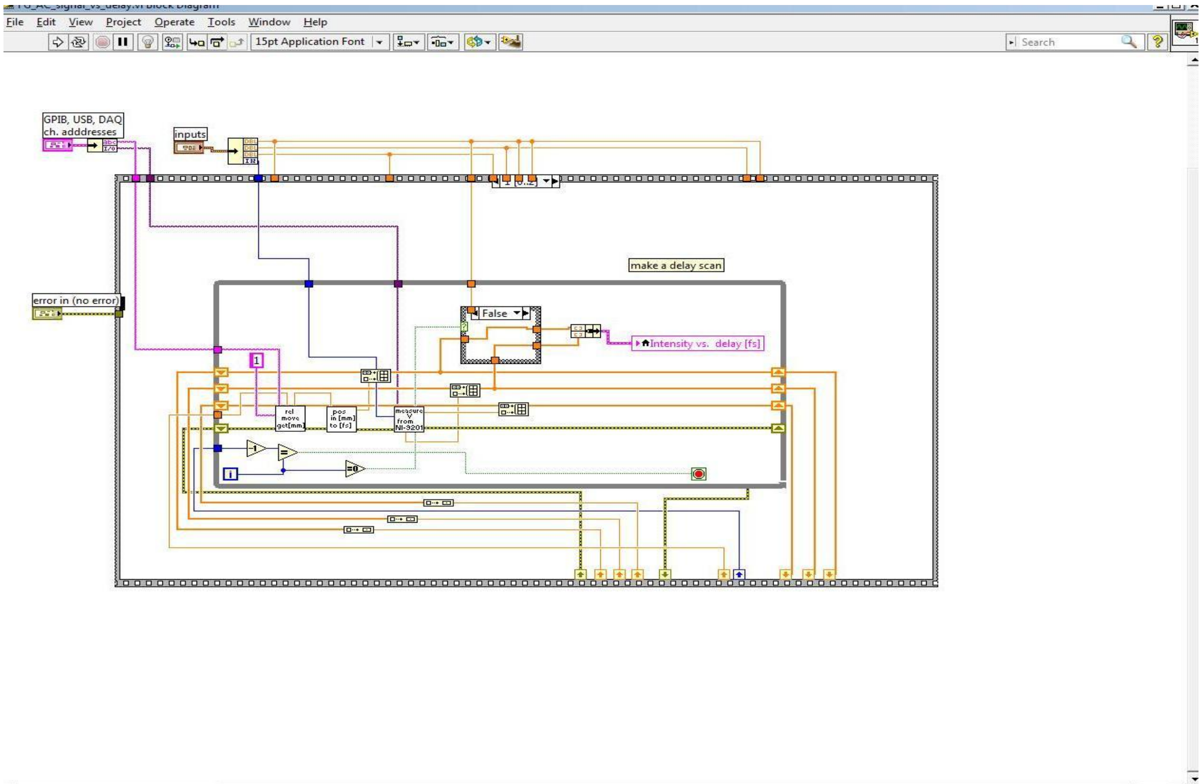

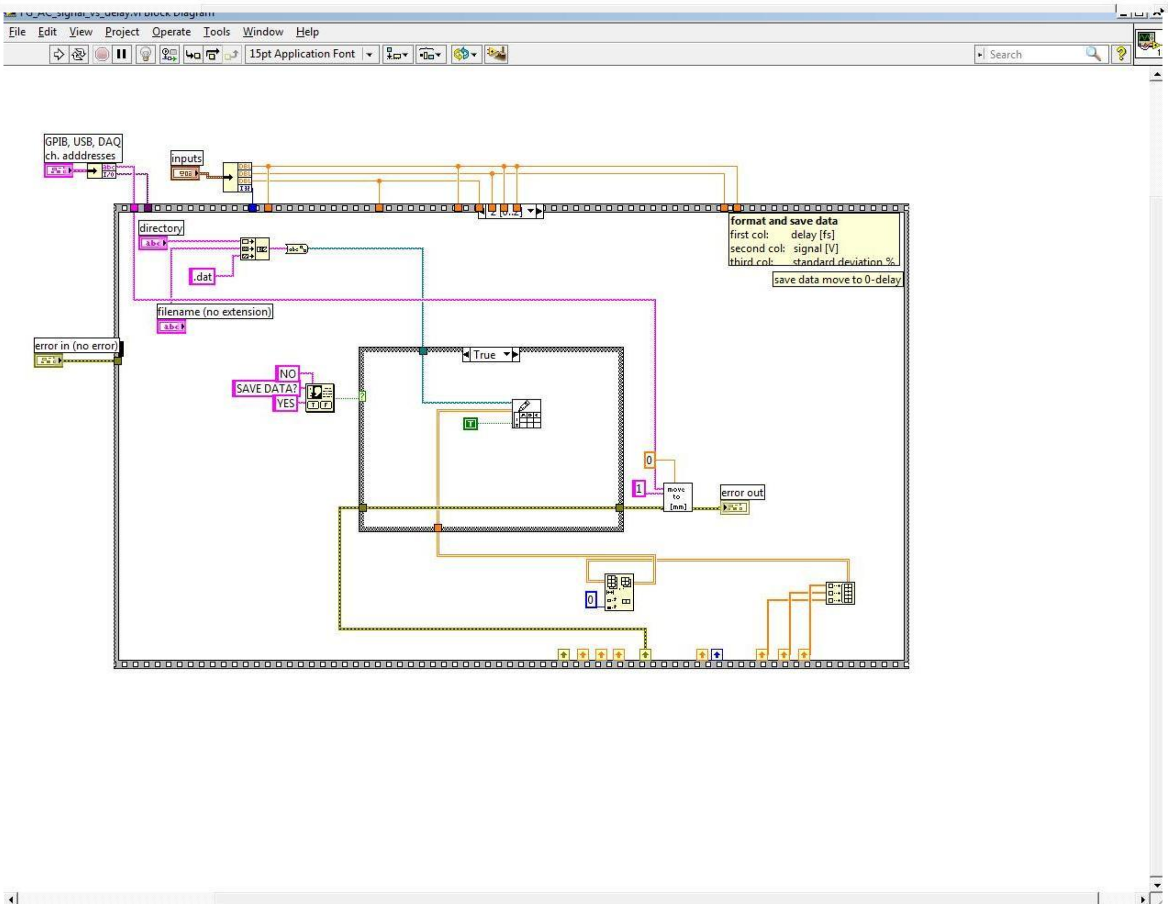

format and save data
first col: delay [fs]
second col: signal [V]
third col: standard deviation %

save data move to 0-delay